Dear Author,

Please, note that changes made to the HTML content will be added to the article before publication, but are not reflected in this PDF.

Note also that this file should not be used for submitting corrections.

Journal of Power Sources xxx (2015) 1–18

Contents lists available at ScienceDirect

Journal of Power Sources

journal homepage: www.elsevier.com/locate/jpowsour

Review

Materials and fabrication of electrode scaffolds for deposition of MnO_2 and their true performance in supercapacitors

Jianyun Cao [a, b], Xiaohong Li [b, c, **], Yaming Wang [a, *], Frank C. Walsh [b], Jia-Hu Ouyang [a], Dechang Jia [a], Yu Zhou [a]

[a] Institute for Advanced Ceramics, Harbin Institute of Technology, Harbin 150001, China
[b] Electrochemical Engineering Laboratory, Energy Technology Group, Faculty of Engineering and the Environment, University of Southampton, Southampton SO17 1BJ, UK
[c] Renewable Energy Group, College of Engineering, Mathematics and Physical Sciences, University of Exeter, Penryn Campus, Cornwall TR10 9FE, UK

HIGHLIGHTS

- Designs, materials and fabrications for binder-less MnO_2 electrode are reviewed.
- True performances of the MnO_2 electrode architectures are evaluated.
- Poor loading of MnO_2 and large dead volume ratio inhibit the practical application.
- Possible ways to bring MnO_2 electrodes to real-world applications are considered.

GRAPHICAL ABSTRACT

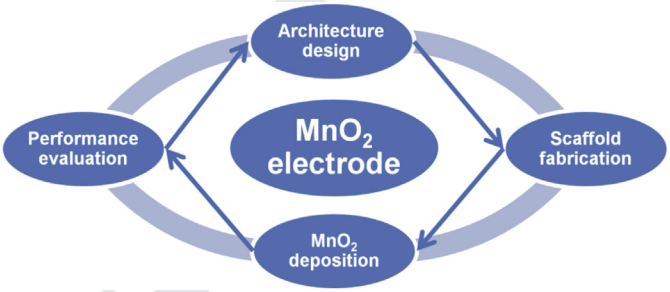

ARTICLE INFO

Article history:
Received 31 March 2015
Received in revised form
25 May 2015
Accepted 28 May 2015
Available online xxx

Keywords:
Manganese dioxide
Supercapacitor
Electrode structure
Deposition

ABSTRACT

MnO_2 is a promising electrode material for high energy supercapacitors because of its large pseudo-capacitance. However, MnO_2 suffers from low electronic conductivity and poor cation diffusivity, which results in poor utilization and limited rate performance of traditional MnO_2 powder electrodes, obtained by pressing a mixed paste of MnO_2 powder, conductive additive and polymer binder onto metallic current collectors. Developing binder-free MnO_2 electrodes by loading nanoscale MnO_2 deposits on pre-fabricated device-ready electrode scaffolds is an effective way to achieve both high power and energy performance. These electrode scaffolds, with interconnected skeletons and pore structures, will not only provide mechanical support and electron collection as traditional current collectors but also fast ion transfer tunnels, leading to high MnO_2 utilization and rate performance. This review covers design strategies, materials and fabrication methods for the electrode scaffolds. Rational evaluation of the true performance of these electrodes is carried out, which clarifies that some of the electrodes with as-claimed exceptional performances lack potential in practical applications due to poor mass loading of MnO_2 and large dead volume of inert scaffold materials/void spaces in the electrode structure. Possible ways to meet this challenge and bring MnO_2 electrodes from laboratory studies to real-world applications are considered.

* Corresponding author.
** Corresponding author. Electrochemical Engineering Laboratory, Energy Technology Group, Faculty of Engineering and the Environment, University of Southampton, Southampton, SO17 1BJ, UK.
E-mail addresses: X.Li@exeter.ac.uk (X. Li), wangyaming@hit.edu.cn (Y. Wang).

http://dx.doi.org/10.1016/j.jpowsour.2015.05.115
0378-7753/

1. Introduction

1.1. Supercapacitors

Supercapacitors (also known as electrochemical capacitors or ultracapacitors), which combine the advantages of high power density (>10 kW kg^{-1}) for short time power uptake and delivery (10^{-1}–10^{2} s) and long shelf life and cycle life (>500,000 cycles), are a competitive solution to electrical energy storage in various applications (from miniaturized portable electronic devices to electric vehicles) [1–5]. The most representative example is the application of electrochemical double layer capacitors (EDLCs) in the emergency doors on the Airbus A380 jumbo-jet [4], demonstrating the high reliability of supercapacitors. The commercialized EDLCs store electric energy by reversible adsorption/desorption of ions on the surfaces of the electrode materials (typically carbon) [6], thus show a limited energy density of 3–8 Wh kg^{-1} (the energy density for Li-ion batteries is generally >100 Wh kg^{-1}) [2,4,7]. With the ever increasing requirements for supercapacitors in many present and future applications, more and more energy is needed to be stored/released in one charging/discharging cycle [5].

Pseudo-capacitors which utilize the fast redox reactions occurring at the surface and bulk of the electrode materials are able to give a much larger energy density when compared with EDLCs [4,7–9]. Typical pseudo-capacitive materials are transition metal oxides (RuO_2, MnO_2, NiO, Co_3O_4, etc.), as well as conducting polymers (polyaniline, polypyrrole, polythiophene and their derivatives) [8–10]. Among these pseudo-capacitive materials, MnO_2, characterized by high theoretical specific capacitance, low costs, natural abundance and environmentally friendliness, is the most widely researched pseudo-capacitive materials for developing high energy supercapacitors over the last decade, several reviews having been published [4,8,11–13].

1.2. The pseudo-capacitance mechanism in MnO_2

MnO_2 stores the charges mainly by pseudo-capacitive (Faradic) reactions occurring at the surface and bulk of the solid MnO_2 phase according to [4]:

$$\mathrm{Mn(IV)O_2} + x\mathrm{C^+} + y\mathrm{H^+} + (x+y)\mathrm{e^-} \leftrightarrow \mathrm{Mn(III)}_{(x+y)},\ \mathrm{Mn(IV)}_{1-(x+y)}\mathrm{OOC}_x\mathrm{H}_y \quad (1)$$

where $C^+ = Li^+, Na^+, K^+$. For the surface pseudo-capacitive reaction, charge storage is realized by adsorption/desorption of electrolyte cations and protons on the surface of MnO_2 [14–16]. For the bulk (subsurface) pseudo-capacitive reaction, charge storage is achieved by the intercalation/deintercalation of protons and cations into the bulk of the MnO_2 [14,17]. However, due to the poor electronic conductivity and slow proton and cation diffusivity of the solid MnO_2 phase [14], the bulk pseudo-capacitive reaction is limited into a thin subsurface layer of MnO_2, for instance, *ca.* 420 nm in thickness according to Bélanger's study [14]. Nevertheless, the fast, reversible successive surface and subsurface redox reaction define the behaviour of the voltammetry close to that of the double layer capacitance in neutral aqueous electrolyte (Fig. 1) [4], which is characterized by a well-defined rectangular shaped cyclic voltammetry (CV) curve. In Fig. 1, the positive half (red (in the web version) in colour) of the CV curve represents the charge/desorption/deintercalation while the negative half (blue (in the web version) in colour) represents the discharge/adsorption/intercalation process. The dashed ellipses depict the fast, reversible successive redox reaction of MnO_2 takes place all through the potential range.

Both surface and bulk pseudo-capacitive charge storage mechanisms are related to the change of Mn oxidation state between Mn(IV) and Mn(III). Assuming that every Mn atom in the electrode is involved in the pseudo-capacitive charge storage, the theoretical specific capacitance of MnO_2 can be calculated by Equation (2) based on one electron per Mn atom involved in the pseudo-capacitive reaction [18].

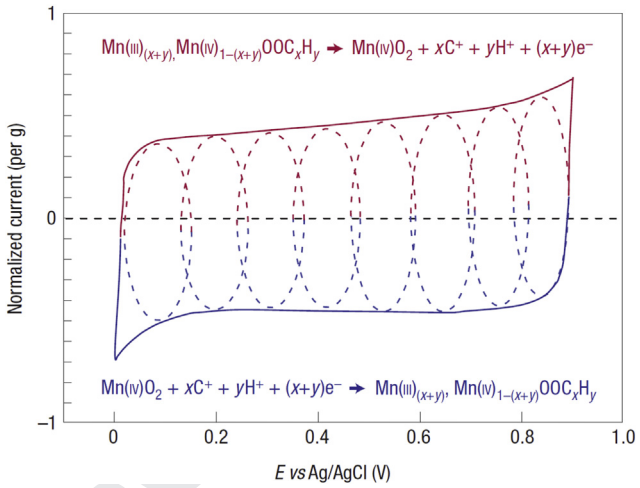

Fig. 1. Schematic of cyclic voltammetry for a MnO_2 electrode in mild aqueous electrolyte. Adapted with permission from Ref. [4]. Copyright (2008) Nature Publishing Group.

$$C = \frac{n \times F}{M \times V} \quad (2)$$

where n is the mean number of the electrons transferred in the redox reaction, and here is one electron per Mn atom, F is the Faraday constant (96 485 C mol^{-1}), M is the molar mass of MnO_2 (86.94 g mol^{-1}) and V is the operating voltage window (0.8 V). On this basis, the calculated, theoretical specific capacitance of MnO_2 is 1387 F g^{-1}.

1.3. Asymmetric supercapacitors based on MnO_2 electrodes

In addition to the high capacitance behaviour of MnO_2, the working potential window of MnO_2 is between 0 and 1.0 V in neutral aqueous electrolytes, which is complementary with that of carbon electrodes (−1.0 to 0 V) [19–22]. Hence, neutral aqueous asymmetric supercapacitors with a MnO_2 electrode as positive electrode and a carbon electrode as negative electrode could achieve a high cell voltage of 1.6–2.0 V, which is twice the value of symmetric supercapacitors in aqueous electrolyte (0.8–1.0 V) [22]. The increased cell voltage could boost the energy density of supercapacitors to a certain high level according to equation:

$$E = \frac{1}{2}CV^2 \quad (3)$$

where E is the energy density, C is the specific capacitance, V is the operating cell voltage.

The asymmetric system was first reported by Hong et al., in 2002 [23], followed by series extensive work conducted by Bélanger [20,24] and Béguin [19,21], which thoroughly studied its charge–discharge mechanism, cell voltage optimization, mass balance and long-term cycling stability. The low-cost and environmental friendly MnO_2-carbon asymmetric system combines the high capacitance of neutral aqueous electrolyte with high cell voltage, is competitive green alternative to the commercial EDLCs based on

organic electrolyte [4]. Hence, developing high energy density asymmetric supercapacitor by using nanostructured MnO_2 electrode with large specific capacitance and high rate capability have attracted great research attention, recently [25–29].

1.4. Limitations of powder and thin film MnO_2 electrodes

As shown in Fig. 2, four factors have significant influences on the electrochemical performances of a MnO_2 electrode: (1) cation diffusion in solid MnO_2 phase; (2) cation diffusion/electrolyte penetration in/through the electrode (depends on the pore structures of the electrode); (3) electron transfer in the solid MnO_2; (4) electron transfer through the electrode (depends on the conductive networks of the electrode). The whole process of the redox reaction could be described as follows based on the four factors: Firstly, the cations in the bulk electrolyte diffuse into the inner layer of the electrode through the pore structures; Secondly, the cations diffuse from the surface of the solid MnO_2 to the bulk reaction site, where redox reaction takes place; Thirdly, the as-generated electrons by the redox reaction transfer through the solid MnO_2 from reaction site to the conductive networks; Finally, electrons transfer though the conductive networks, and are collected by the current collector. Unfortunately, the poor electron conductivity and cation diffusivity of the solid MnO_2 phase is well-known, and hard to be enhanced. A more feasible route for developing high performance MnO_2 electrodes is the design of electrode architectures having uninterrupted cation diffusion channels/pores and electron transfer conductive networks.

For conventional powder electrodes, the reported specific capacitance is far below the theoretical value, <300 F g^{-1} in most cases [11]. A recent mathematical simulation combined with experimental data indicated that only 9% of Mn atoms are involved in the pseudo-capacitive redox reaction in a conventional powder electrode [18], which is characterized by pressing a mixed paste of MnO_2 powder, carbon black and polymer binder onto metallic current collector [7]. To increase the MnO_2 utilization in powder electrodes, efforts have been focused on (1) nanostructuring the MnO_2 particle size to shorten the electron/cation transfer length in solid phase; (2) employing MnO_2 with various crystal structures (α-, β-, γ-, δ- and λ-type) thus different electronic and ionic conductivities [30–32]; (3) doping the MnO_2 with other metal elements (Ni, Fe, Co, V, Mo, Al, Pb or Ru) to achieve better electrical conductivity and charge-storage capability by introducing more defects and charge carriers; (4) anchoring the MnO_2 on carbon substrate, such as carbon black, graphene, carbon nanotubes (CNTs), etc., to enhance the electrical conductivity. There are extensive reviews that cover the advances in the nanosized, crystalline, doped and composited MnO_2 powder electrodes [8,11]. Once being processed into powder electrodes, the advantages of these MnO_2-based materials cannot be fully realized since: (1) the mixed composite paste lacks well interconnected pore structures for electrolyte penetration/ion diffusion through the electrodes and fast long-range electron transfer routes; (2) electrical insulating polymer binder may disrupt the long-range electron transfer through the electrodes [7].

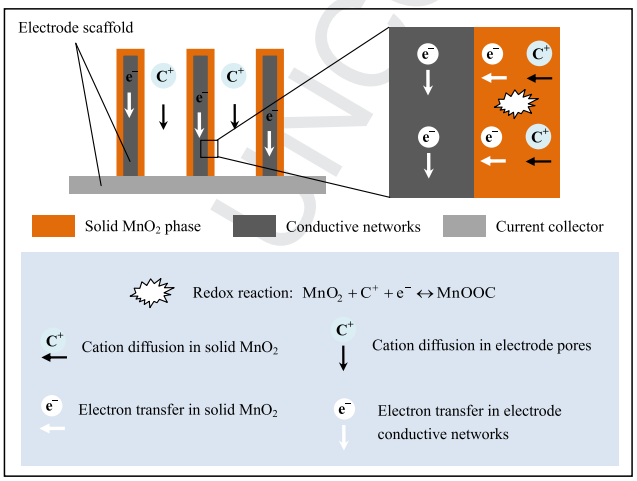

Fig. 2. Schematic of electron and cation transfer in a simplified MnO_2 electrode.

Thin film MnO_2 electrodes can be fabricated by deposition of MnO_2 on traditional current collectors (metal sheets, ITO/FTO glass, nickel foam, etc.) [14,17,33–39]. Thin films with various morphologies (nanoparticles, nanowires, nanorods, nanotubes, etc) and macro/meso-pore structures formed on the surface of the current collectors could allow fast penetration of electrolyte into the entire electrode, thus increasing the accessible surface area for the pseudo-capacitive reaction. The specific capacitance of a ultra-thin film MnO_2 electrode with minute MnO_2 mass loading (5 μg cm^{-2}) could reach 1380 F g^{-1}, approaching the theoretical value [14]. However, thin film electrodes with small mass loading lack the potentials in practical applications due to limited areal capacitance (capacitance normalized by the unit area of the electrode, F cm^{-2}). Efforts to increase the mass loadings of the thin film electrodes thus acceptable areal capacitances were hindered by the lack of fast electron transfer routes in single phase MnO_2 thin films [35]. Actually, the specific capacitance of the thin film MnO_2 electrodes with reasonable mass loading seldom exceeds 300 F g^{-1} [40], except for electrodes with ultrathin MnO_2 films of very low mass loadings [14,17].

1.5. MnO_2 electrodes having designed architecture

Hence, more advanced designs for the architectures of MnO_2 electrodes are needed to achieve the full benefits of high pseudo-capacitance. Recently, more and more research efforts are concentrated on the binder-less architecture-designed MnO_2 electrodes, which are characterized by direct deposition of nanoscale MnO_2 coating within or onto macro-scale device-ready electrode scaffolds with un-interrupted electron pathways and ion diffusion routes [7,41]. The design strategies for the electrode architectures could be classified as core–shell hybrid structures [42,43], nanostructured current collectors [44–47], and flexible textile/paper/fibre electrodes [48–50].

(1) Core-shell hybrid arrays directly connected on the current collectors provide direct one-dimensional (1D) pathways for electron transport, and the void spaces between each nanowire/rod serve as fast ion transport routes after easy electrolyte penetration.
(2) Loading MnO_2 with confined thickness into nanostructured current collectors is an effective way to fully utilize the high pseudo-capacitance. The increased contact area of MnO_2 with the nanostructured current collector could minimize the internal resistance of the electrodes, leading to high power capability.
(3) In addition to requirements of energy storage and management for an energy storage device, additional functionalities (flexible, wearable, transparent, etc.) are demanded due to the development of modern electronic systems [51–57]. Among different multifunctional energy storage systems, flexible supercapacitors have attracted numerous attentions due to the high power and long life merits [51,52,58]. To achieve high energy density, nanoscale MnO_2 has been

widely introduced into the flexible electrode architectures to enhance the capacitance.

Diverse materials have been employed to fabricate the electrode scaffolds for loading MnO_2 in the past decade, such as metals (gold, manganese and nickel) [47,59,60], metal oxide/nitrides (ZnO, TiO_2, TiN and Co_3O_4) [42,43,61–64], carbons (CNTs, graphene and carbon fibres) [28,44,45,49,65,66], conducting polymers (polyaniline, polypyrrole and polythiophene) [67–69], etc. An impressive increase in performance has been achieved with these MnO_2 electrodes thanks to the use of new electrode scaffold materials and design of new scaffold structures, as well as the improved MnO_2 loading technics, namely, electrodeposition and *in-situ* redox deposition.

Nevertheless, some of the as-reported outstanding performances may be not applicable in practical supercapacitors [70]. For the practical supercapacitors, the performances (specific capacitance, energy density, power density, etc.) are always tested with fully packaged cells and normalized by the total weight/volume of the devices (including the active materials, binder, current collector, electrolyte, package, etc.). However, for most of the currently reported MnO_2 electrodes and the as-assembled devices, the values of performances are normalized by the mass of MnO_2 only. Moreover, some important information about the electrodes/devices (MnO_2 mass loading, total weight, geometric dimension, etc.) are not reported. In most cases, the as-reported high specific capacitance and energy density are based on the limited mass of MnO_2 loadings from several tens to hundreds of micrograms, which account very small portion of the total weight of the electrodes/devices. Besides, test fixture configurations (three-electrode and two-electrode), parameters as scan rates and discharge current densities, calculations to reduce the data to the desired metrics are all factors that will cause uncertainties in performance values [71]. As a result, the widely varied performance results present difficulty in rational evaluating and comparing the true performance of MnO_2 electrodes/devices.

Several reviews cover different aspects of MnO_2 based materials for supercapacitors [4,7–9,11–13,25,40,72]; to the best of our knowledge, none of them focuses on the binder-less MnO_2 electrodes prepared by deposition of nanoscale MnO_2 on prefabricated, device-ready electrode scaffolds. In addition, rational evaluation of the true performance of these MnO_2 electrodes is both important and urgent.

Here, we provide a timely review, which covers the four processes for developing MnO_2 electrodes with designed architecture (Fig. 3): (1) the design strategies, (2) materials and fabrication methods for the electrode scaffolds, (3) methods for deposition of MnO_2 on the electrode scaffolds, (4) performance evaluation. The design strategies have already been summarized earlier in this section. The rational evaluation of the true performance of the MnO_2 electrodes will be discussed prior in section 2 due to its importance. Section 3 provides a comprehensive review of materials and fabrication of electrode scaffolds. The methods for deposition of MnO_2 are summarized at last.

2. True performances of MnO_2 electrodes

With the expansion of research interests in MnO_2 based electrodes, numerous electrodes and as-assembled devices with various specific capacitances (from 100 to 1200 F g^{-1}) and energy densities (from ~5 to 150 W h kg^{-1}) have been reported, causing marked difficulty in comparing performances and determining true benefits of these electrodes and devices. In this section, we will rationally evaluate the performance of the architecture-designed MnO_2 electrodes and as-assembled devices by comparison to that of conventional MnO_2 powder, thin film electrodes and commercial, activated carbon electrodes and devices.

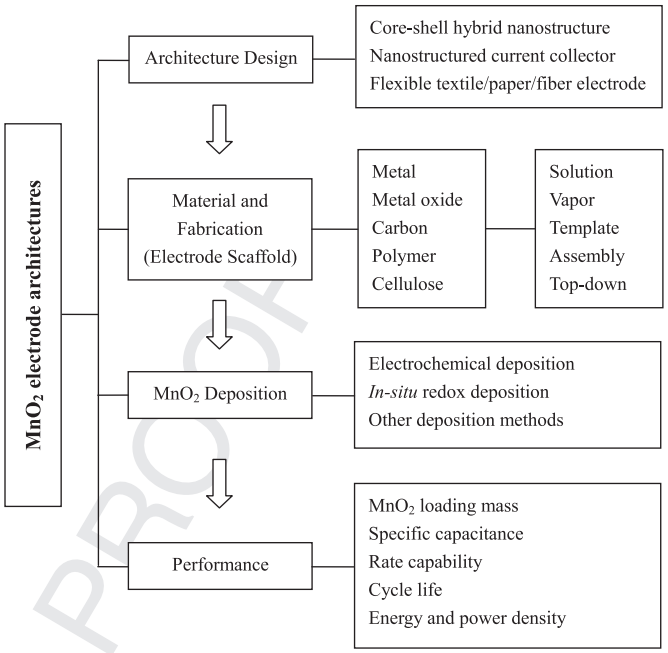

Fig. 3. Four processes for developing MnO_2 electrodes with designed architecture.

2.1. MnO_2 mass loading and specific capacitance

Before evaluating the performances of a MnO_2 electrode, the relationship between MnO_2 mass loading and specific capacitance has to be clearly understood. A typical example of the influences of MnO_2 mass loading on the specific capacitance and areal capacitance are shown in Fig. 4 [66]. The specific capacitance *vs.* scan rate of three-dimensional (3D) graphene/MnO_2 composite network electrodes with different MnO_2 mass loadings are shown in Fig. 4a. The specific capacitance gradually decreases with a higher MnO_2 mass loading from 0.1 to 9.8 mg cm^{-2} at all scan rates because of the poor ionic and electronic conductivity of MnO_2. In contrast, the areal capacitance increases at higher MnO_2 mass loading without saturation at scan rates below 20 mV s^{-1} in Fig. 4b while, at fast scan rates of 50–200 mV s^{-1}, a critical value appears at about 3.3 mg cm^{-2} which is probably due to the critical cation diffusion length in the MnO_2 phase at these scan rates. Similar trends were also reported in other literature [47,73–75]. By understanding the significant influence of MnO_2 mass loading on the capacitance behaviour of MnO_2 electrodes, it is clear that reporting specific capacitance without mass loading can mislead researchers in evaluating the real values of such electrodes.

Table 1 summarizes the specific capacitances of some typical MnO_2 electrodes. For benchmarking the performances, specific capacitances of typical activated carbon (AC), MnO_2 powder electrode, graphene/MnO_2 composite powder electrode and thin film MnO_2 electrodes on planar conductive substrates with MnO_2 mass loading from 0.005 to 4.5 mg cm^{-2} are also shown in Table 1.

2.1.1. Powder electrodes

For the powder electrodes, MnO_2/graphene composite powder (78 wt.% MnO_2) mixed with carbon black and PTFE binder with a mass ratio of 75:20:5 was coated onto the nickel foam substrate with a mass loading of 3 mg cm^{-2} (which is 2.25 mg cm^{-2} for the active material) [76]. The graphene/MnO_2 composite powder electrode delivered a specific capacitance of 310 F g^{-1} and an areal

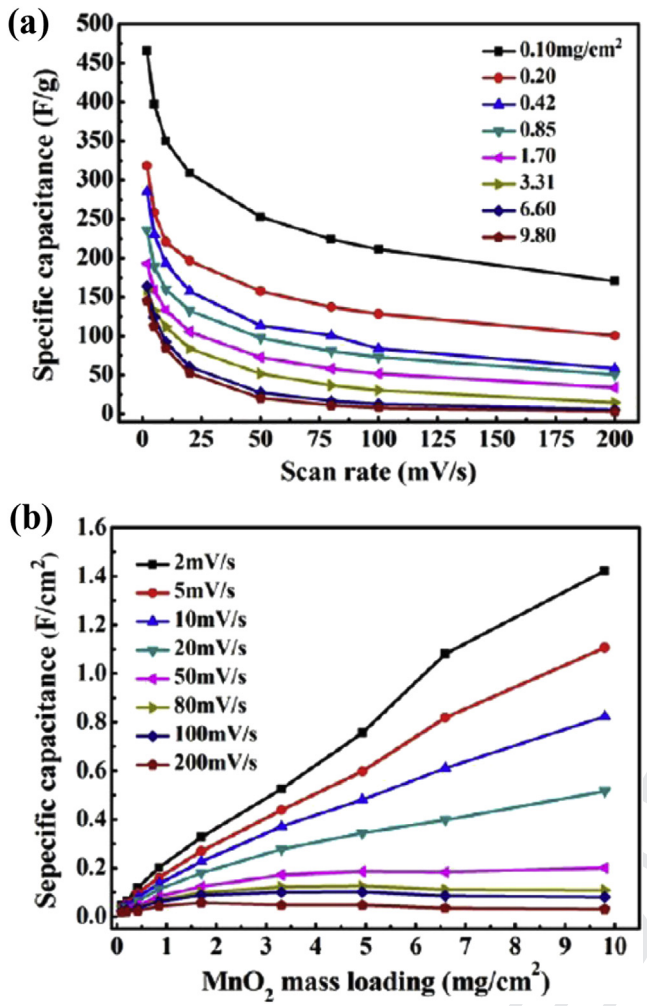

Fig. 4. (a) Specific capacitance *vs.* scan rate for samples with different mass loadings of MnO_2. (b) Areal capacitance *vs.* mass loading of MnO_2 at different scan rates. Adapted with permission from Ref. [66]. Copyright (2013) American Chemical Society.

capacitance of 697.5 mF cm^{-2} if normalized by the footprint of the electrode based on the as-reported data [76].

2.1.2. Thin film electrodes

For thin film electrodes, ultra-small MnO_2 mass loading of 5 μg cm^{-2} led to a high specific capacitance of 1380 F g^{-1}, approaching the theoretical value [14]. However, the area normalized capacitance of 6.9 mF cm^{-2} is far away from the value of powder electrode, indicating the lack of potential in practical application for such electrodes with ultra-small MnO_2 mass loading. Increasing the mass loading of the thin film electrodes from 0.005 mg cm^{-2} to different orders of magnitude of 0.05, 0.41 and 4.5 mg cm^{-2} resulted in a significant decrease in specific capacitance especially under high rate conditions. The thin film electrode with a mass loading of 4.5 mg cm^{-2}, which is comparable with that of the powder composite electrode (~3 mg cm^{-2}), could only deliver a poor specific capacitance <75 F g^{-1} and a relative small areal capacitance of ~350 mF cm^{-2} [35]. Hence, these thin film electrodes built on flat substrate could hardly be scaled up to large energy storage systems, but for interests of fundamental research, micro-devices and on-chip energy storage systems.

2.1.3. Architecture-designed electrodes vs. thin film electrodes

For architecture-designed MnO_2 electrodes based on various electrode scaffolds, the electrode scaffolds with increased surface area, interconnected conductive networks and pore structures could allow a much higher MnO_2 mass loading than planar substrate while maintaining good capacitance behaviour.

As summarized in Table 1, electrode architectures with MnO_2 mass loading below 1 mg cm^{-2} exhibited excellent specific capacitances around 1000 F g^{-1}, which are much better than that of the thin film electrodes with MnO_2 mass loading at the same order of magnitude. For example, MnO_2 deposited on CNTs coated sponge with a mass loading of 0.05 mg cm^{-2} could deliver a capacitance of 1230 F g^{-1} [73], while MnO_2 deposited on stainless steel foil with the same mass loading could only deliver a capacitance of 412 F g^{-1} [34]. For the electrodes with mass loading above 1 mg cm^{-2}, the advantage of architecture-designed electrodes when compared with thin film MnO_2 electrodes is also obvious. MnO_2 deposited on CNTs arrays grown on carbon cloth with a high mass loading of 4.09 mg cm^{-2} could deliver a specific capacitance of 326 F g^{-1} at 2 mV s^{-1} [75], which is much larger than that of thin film MnO_2 on graphite disk (75 F g^{-1}) with a comparable mass loading of 4.5 mg cm^{-2} [35]. Even when the mass loading is increased to as high as 9.8 mg cm^{-2} with a 3D graphene networks scaffold, the specific capacitance base on the total mass of the entire electrode (150 F g^{-1}) is twice as large as that of thin film MnO_2 on the graphite disk [66].

2.1.4. Architecture-designed electrodes vs. powder electrodes

Despite these as-reported ultrahigh specific capacitances based on electrodes with mass loadings less than 1 mg cm^{-2}, the poor areal capacitances (<400 mF cm^{-2}) when compared with that of the graphene/MnO_2 composite powder electrode (697.5 mF cm^{-2}) [76] and commercial, activated carbon electrode (1600 mF cm^{-2}) [70,77] dramatically limit their application in real supercapacitors. Most of the metal and metal oxide array based electrode scaffolds could not afford MnO_2 mass loading higher than 1 mg cm^{-2} due to the limited thickness of such scaffolds. In addition, electrodes with extremely thin thickness and/or very minute amounts of active material could lead to an overestimation of the specific capacitance according to Ruoff's view [71]. On the other hand, some of the electrode architectures lose the capacitance advantage when compared with the powder electrodes, such as MnO_2 deposited on carbon nanofibre paper with a MnO_2 mass loading of *ca.* 2.2 mg cm^{-2} could only deliver a comparable capacitance of 320 F g^{-1} and further increase the mass loading to 3.41 mg cm^{-2} led to the decrease of specific capacitance to 188 F g^{-1} [65], which is just comparable with that of the MnO_2 powder electrode (203 F g^{-1}) [15] and commercial activated carbon electrode (160 F g^{-1}) [77].

As further improvement of the performance of powder electrodes is limited by the *ad-hoc* nature resulted from its fabrication process as discussed in the very beginning of this review, developing electrode scaffolds which could afford MnO_2 mass loading larger than 1 mg cm^{-2}, even approaching that of commercial activated carbon electrodes (10 mg cm^{-2}), while maintain the reasonable high specific capacitance and rate capability is both challenging and urgent for material scientists.

Generally, scaffolds with large thicknesses, such as CNTs arrays on Ta foil (35 μm) [45], CNTs arrays on carbon cloth (50 μm) [75], 3D graphene networks (*ca.* 200 μm) [66] and carbon nanofoam paper (230 μm) [46] could afford high MnO_2 mass loading while maintain a reasonable good specific capacitance performance and rate capability. Besides, combining MnO_2 with conducting polymer, like PPy [78,79], to form core–shell hybrid structures could also achieve high specific capacitances at relatively high MnO_2 mass loadings.

Another advantage of architecture-designed MnO_2 when compared with commercial activated carbon electrodes is the high

Table 1
Mass loadings and specific capacitances of various MnO_2 electrodes.

Electrode scaffold	Loading/mg cm^{-2}	C_m/F g^{-1}	C_A/mF cm^{-2}	C_V/F cm^{-3}	Ref.
Commercial activated carbon electrode					
Al foil	10	160 (aqueous)	1600	112	[70,77]
MnO_2 powder electrode					
Ta foil	N/A	203 at 2 mA cm^{-2}			[15]
Graphene/MnO_2 composite powder electrode					
Ni foam	2.25	310 at 2 mV s^{-1}	697.5 at 2 mV s^{-1}		[76]
MnO_2 thin film electrodes					
Pt substrate	0.005	1380 at 5 mV s^{-1}	6.9 at 2 mV s^{-1}		[14]
Stainless steel foil	0.05	412 at 2 mV s^{-1}	20.6 at 2 mV s^{-1}		[34]
Stainless steel foil	0.41	320 at 20 mV s^{-1}	125 at 20 mV s^{-1}		[36]
Graphite disk	4.5	<75	~350		[35]
Architecture-designed MnO_2 electrodes					
CNTs coated sponge	~0.05	1230 at 1 mV s^{-1}	61.5 at 1 mV s^{-1}		[73]
CNFs forests on 3D graphene	0.1	946 at 2 mV s^{-1}	330 at 1 mA cm^{-1}		[183]
H–ZnO nanowire arrays	0.11	1260 at 1 mA cm^{-2}	138 at 1 mA cm^{-2}		[107]
3D macroporous Mn	~0.32	1200[a] at 5 mV s^{-1}	372 at 5 mV s^{-1}		[85]
Nanoporous Au	40 wt.%	1145 at 50 mV s^{-1}		1160	[47]
CNTs sponge	39.1 wt.%	325[a] at 2 mV s^{-1}		16.1	[82]
Graphene/CNTs composite paper	1.13	326 at 10 mV s^{-1}		130	[89]
Co_3O_4 nanowire arrays	1.5	480 at 2.67 A g^{-1}	560 at 11 mA cm^{-2}		[63]
Hollow Ni dendrites	1.8	303 at 5 mV s^{-1}	545 at 5 mV s^{-1}		[60]
PPy coated CNFs paper	2.0	705 at 2 mV s^{-1}	1400 at 2 mA cm^{-2}		[78]
CNFs paper	3.41	188 at 2 mV s^{-1}			[65]
CNTs arrays on carbon cloth	4.09	326 at 2 mV s^{-1}	2081 at 0.1 mV s^{-1}		[75]
Graphene-gel coated Ni foam	6.11	245 at 10 mV s^{-1}	1500 at 10 mV s^{-1}		[163]
CNTs array on Ta foil	6.7	~150[a]		299	[45]
3D graphene networks	9.8	130[a] at 2 mV s^{-1}	1420 at 2 mV s^{-1}		[66]
Carbon nanofoam paper	60 wt.%	150[a]	7500	280	[46]

Note: C_m is specific capacitance; C_A is areal capacitance; C_V is volumetric capacitance.
[a] The capacitance is based on the total mass of the scaffold and MnO_2.

volume normalized capacitance. This is because the incorporation of nanoscale MnO_2 within the nanoporous electrode scaffolds will not change the volume of the scaffolds. For instance, incorporating of MnO_2 within the free-standing nanoporous gold sheets (100 nm in thickness) led to an ultrahigh volumetric capacitance of 1160 F cm^{-3} at 50 mV s^{-1} [47]; incorporation of homogeneous nanoscale MnO_2 into nanofoam paper with thickness (230 μm) comparable to that of commercial carbon electrodes (100–200 μm) also led to a good volumetric capacitance of 280 F cm^{-3} [46], more than twice of that value of commercial activated carbon electrodes (112 F cm^{-3}) [77]. However, for electrode scaffolds with ultraporous structures thus very small packing densities, like CNTs sponge (10–20 mg cm^{-3}) [80], graphene aerogel (0.16 mg cm^{-3}) [81], are hardly to be able to achieve high volumetric capacitance due to the large portion of dead volume (excess pore volume) in the electrodes. For instance, the CNT-PPy-MnO_2 nanotube sponge could only give a small volumetric capacitance of 16.1 F cm^{-3} even with 50% compression [82]. Even worse, the excess empty space in the electrode will be flooded by electrolyte, thus increasing the weight of the electrode without adding any capacitance [70]. Thus, an appropriate type and degree of porosity is critical to achieve high volumetric capacitance.

Moreover, some seemingly mediocre specific capacitances reported in the literature when compared with that of the powder electrode are actually normalized by the total mass of the electrodes (including the self-support carbon scaffolds) [28,82]. In powder electrodes, the need of using heavy weight metal current collectors accounts most of the weight of the electrode, and the specific capacitance based on the total mass of the electrodes could be much smaller than that normalized by the mass of the active materials.

It is worth noting that some of the extremely high reported area normalized specific capacitances (up to 2800 mF cm^{-2}) of MnO_2 electrodes are obtained from very slow potential scan rates: 0.05–0.1 mV s^{-1} or at low current densities: 0.2 mA cm^{-2} [74,75,79], which is not appropriate to reflect the true performance of electrodes for supercapacitor applications. For example, the charging/discharging time for an electrode working at potential range of 0–0.8 V under a scan rate of 0.05 mV s^{-1} will be 16,000 s (about 4.4 h), which is far away from the time scale of supercapacitors (10^{-1}–10^2 s) [7].

2.2. Energy density and power density

Energy density and power density are two key metrics for evaluating the performance of a supercapacitor device. Table 2 summarizes the energy densities and power densities of some typical devices based on architecture-designed electrodes, including both symmetric and asymmetric systems. For the purpose of rational evaluating (benchmarking) the performances of these devices, the energy density and power density of a commercial Maxwell device (BCAP0001: 1 F; 2.7 V) [83] is also shown in Table 2. The as-reported energy densities of these supercapacitor devices vary in a large range from 2.2 to 67.5 Wh kg^{-1}, making comparison of these devices difficult. The main reason for the large range in the as-reported energy density and the as-resulted difficulties for comparison of the literature reported energy density are the lack of well standardized test configurations, measurement procedures and data reporting rules. Detailed reasons are listed below.

(1) Energy density which is calculated by the single electrode capacitance tested with a three-electrode configuration is four-fold larger than that calculated by the device capacitance tested with a two-electrode configuration [42,84–86]. In some literature, although the test configuration is two-electrode cell, the calculation of energy density is carried

Table 2
Energy densities, power densities and cycling stabilities of some typical devices based on architecture-designed MnO_2 electrodes.

Type of electrodes	Loading/mg cm^{-2}	V/V	Energy density	Power density	Lifetime	Ref.
Maxwell commercial device (BCAP0001: 1 F; 2.7 V) Size: 12 (Length) × 8 (Diameter) mm; Weight: 1.1 g						
Activated carbon (AC)	N/A	2.7	0.9[a] Wh kg^{-1} 1.7 mWh cm^{-3}	2400[a] W kg^{-1} 4.4 W cm^{-3}	70% (500,000)	[83]
Symmetric capacitors						
Hollow Ni dendrites@MnO_2	1.8	1.0	9 Wh kg^{-1}	72 kW kg^{-1}	97.2% (4000)	[60]
Nanoporous gold@MnO_2	40 wt.%	0.8	57 W h kg^{-1}	16 kW kg^{-1}	85% (1000)	[47]
H−ZnO_2 nanowire arrays@MnO_2	0.11	0.8	0.04 mW h cm^{-3}	2.44 mW cm^{-3}	87.5% (10,000)	[107]
CNTs coated Sponge@MnO_2	~0.05	1.0	31 W h kg^{-1}	63 kW kg^{-1}	96% (10,000)	[73]
Graphene/CNTs/MnO_2 composite film	56 wt.% 2.02	1.0	8.9 W h kg^{-1} 2.2[a] W h kg^{-1}	170 kW kg^{-1} 42[a] kW kg^{-1}	95% (1000)	[89]
Asymmetric capacitors						
Co_3O_4@ PPy@MnO_2//AC	1.8	1.6	34.3 W h kg^{-1}	12 kW kg^{-1}	100.4% (11,000)	[127]
H−TiO_2@MnO_2//H−TiO_2@C	0.23	1.8	0.3 mW h cm^{-3} 59 Wh kg^{-1}	0.23 W cm^{-3} 45 kW kg^{-1}	91.2% (5000)	[29]
Graphene-gel@MnO_2//Graphene-gel	6.11	1.8	0.72 mW h cm^{-3}	0.4 W cm^{-3}	98.65% (10,000)	[163]
3D graphene@CNTs@MnO_2//3D graphene@CNTs@AC	0.84	2.0	33.71 W h kg^{-1}	22.7 kW kg^{-1}	95.3% (1000)	[182]
CNTs/Au/MnO_2 film//AC (Ionic liquid electrolyte)	1.0	3.0	67.5 W h kg^{-1}	598.8 W kg^{-1}	N/A	[88]

Note: V is the cell voltage.
[a] Energy density or power density based on the total mass of the device.

out with the single electrode capacitance but not the device capacitance [87].

(2) Energy density and power density of the MnO_2 active material are sensitive to the mass loading, just as the specific capacitance that has been discussed above. Device with ultra-small MnO_2 mass loading are easy to achieve high gravimetric energy density and power density, but the high gravimetric energy density and power density are almost irrelevant to the areal and volumetric energy density and power density due to the negligible weight content of MnO_2 in the device.

(3) In most of the literature, important information about the device, such as weight and size of the total device are missing, making the comparison of performance of the whole device impossible. Energy density and power density of commercial devices are always based on the total weight or volume of the whole packaged device. For materials research and development, it is nothing wrong to report the energy density and power density of a supercapacitor device based on the mass of the active materials. It is good practice to report all essential device information, including the total weight, the volume of the device and content of active materials in the device.

Nevertheless, some conclusions can still be drawn from Table 2. Firstly, the energy density of the asymmetric systems is generally higher than that of the symmetric systems due to the increased cell voltage from 0.8−1.0 V (symmetric) to 1.6−2.0 V (asymmetric). The asymmetric system combined with ionic liquid electrolyte further boosted the cell voltage to 3.0 V, and high energy density to 67.5 W h kg^{-1}, however, the cycling stability of such system still needs to be thoroughly understood [88]. Secondly, a rod-shaped supercapacitor assembled by two robust graphene/CNTs/MnO_2 composite films (3.2 mg, 2.2 mg cm^{-2}) without metallic current collector could deliver an energy density of 2.2 W h kg^{-1} and a maximum power density of 42 kW kg^{-1} based on all the components of the packaged cell [89], which are better than that of the commercial device (0.9 W h kg^{-1}; 2400 W kg^{-1}) with comparable size. Finally, in spite of these as-reported high energy densities and power densities normalized by the mass of active materials, the volumetric energy densities (vary from 0.03 to 0.72 mW h cm^{-3}) and power densities (vary from 0.002 to 0.4 W cm^{-3}), which were normalized by the total volume of the devices, are still far away from that of the commercial device (E = 2.68 mW h cm^{-3}; P = 4.4 W cm^{-3}). This is because of most of the electrode architectures are lacking of volume efficiency, the large volume portion of inert scaffold materials and void spaces in the electrodes drags down the energy density of the whole device which only contains a minute amount of active material.

3. Materials and fabrication of electrode scaffolds

As discussed above, the current strategies for the design of MnO_2 electrode architectures are mainly focused on loading MnO_2 on electrode scaffolds, which act both as high surface area mechanical support and current collector for the active MnO_2 phase and are the main physical link between the electrode and the external structures of the supercapacitor. In some occasions, the electrode scaffolds can act as active materials for energy storage themselves, such as carbon nanofoam paper [46] and Co_3O_4 nanowire arrays [63]. Materials for construction of electrode scaffolds for loading of MnO_2 must be discriminated by their:

1) Chemical stability in aqueous electrolytes
2) Electrochemical stability during the charging-discharging process
3) Low density
4) High conductivity
5) Low costs
6) Good processability to form porous structures

Metal and carbon materials are widely used for fabrication of nanostructured current collectors. Metal oxides with relatively better electrical conductivity than MnO_2 usually act as core materials for fabrication of core−shell hybrid nanostructures. Conducting polymers have great potential in fabrication of core-double-shell hybrid structures thanks to their flexibility, high conductivity and good pseudo-capacitance. Conductivity-modified natural cellulose and synthetic fibres are ideal platforms for developing of flexible textile/paper/fibre electrodes.

Numerous methods have been explored to fabricate the electrode scaffolds from both bottom-up and top-down. Bottom-up methods are the major synthesis strategy, including solution-based growth approaches as hydrothermal and electrochemical methods; vapour based growth approaches as chemical vapour deposition

(CVD) method; and bottom-up assembly of CNTs and graphene building blocks. Most of the metal oxide and carbon architectures are synthesized by bottom-up approaches. Top-down procedures are effective methods for fabrication of metal or metal oxide/nitride nanostructures by direct etching/dealloying or oxidation-nitriding of the bulk metal substrates.

3.1. Metals

3.1.1. Nickel

Nickel is widely used as current collector material for aqueous supercapacitors that work in neutral and alkaline medium. Up till now, various nanostructured nickel current collectors have been fabricated and used for deposition of MnO_2, including nanoporous nickel [90–92], nickel nanorod array [93], and nickel hollow dendrites [60]. Methods including electrochemical dealloying [90,94], template assisted electrodeposition [60,93,95] and reduction of nanostructured NiO_2 [91] or $Ni(OH)_2$ [92] precursors were used to fabricate these nickel nanostructures.

3.1.2. Gold

Despite its rarity and high cost, the super chemical stability versus all kind of electrolytes means that gold and its alloys are near-ideal materials for fabrication of nanostructured current collectors. The most representative design based on a nanostructured gold current collector is the nanoporous metal/oxide hybrid electrode conducted by Chen's group [47]. As shown in Fig. 5, a 100 nm thick nanoporous gold film prepared by chemical dealloying was loaded with MnO_2 nanocrystals by a simple redox reaction between N_2H_4 gas and MnO_4^- solution. The SEM image demonstrates that the MnO_2 nanocrystals were uniformly plated into the nanoporous gold without changing the nanoporosity. As a result, the nanoporous metal/oxide hybrid electrode delivered a high volumetric capacitance of 1160 F cm^{-3} at a scan rate of 50 mV s^{-1}. The drawback of the nanoporous gold/MnO_2 hybrid electrode is that the ultra-small thickness of the electrode (100 nm) thus low MnO_2 loading mass cannot provide large enough areal capacitance for real application. Besides, the high cost of gold severely limits its wide use.

In addition to the free-standing nanoporous gold sheets prepared by chemical dealloying [47,96–98], electrochemically grown gold nanowire stems [99], and lithographically patterned gold nanowires [100,101] have also been used as nanostructured current collectors for loading of MnO_2. In some cases, a gold film was sputtered on a pre-fabricated nanostructured scaffold to achieve a reasonable electrical conductivity [102,103].

3.1.3. Manganese

In-situ oxidation of metallic manganese nanostructures gives uniform coating of manganese oxide layer with large contact area and well bonded interface, thus minimizing the interface resistance. Mn nanotube arrays [59] and three-dimensional ordered macro-porous (3DOM) metallic Mn films [85] (prepared by template assisted electrodeposition methods) have been used as supercapacitor electrodes after *in-situ* oxidization to generate a thin layer of MnO_2.

3.1.4. Titanium

Recently, Ti nanowire arrays, which were synthesized by etching Ti substrate in aqueous HCl solution under hydrothermal condition, were also investigated as nanostructured current collector for fabrication of MnO_2 electrodes [104].

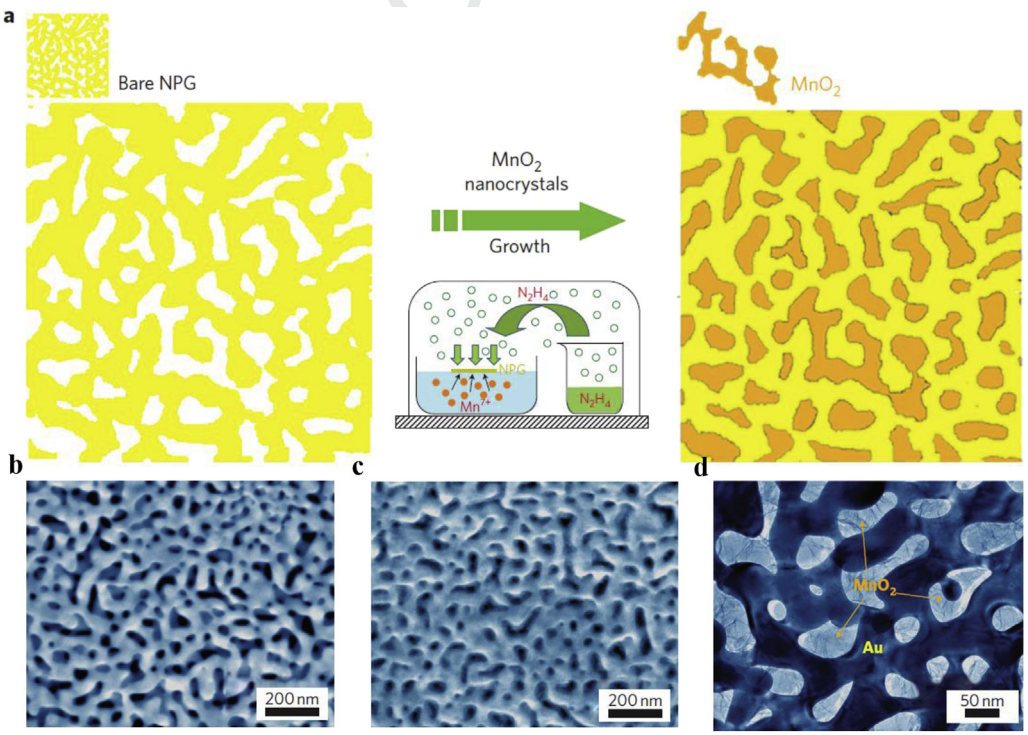

Fig. 5. (a) Schematic showing the fabrication process for nanoporous gold/MnO_2 hybrid materials by directly growing MnO_2 (orange) onto nanoporous gold. (b) SEM image of as dealloyed nanoporous gold films with a characteristic pore length of 40 nm. (c) SEM image of a nanoporous gold/MnO_2 film with a MnO_2 plating time of 10 min. MnO_2 nanocrystals were uniformly plated onto the gold without changing the nanoporosity. (d) Bright-field TEM image of the nanoporous gold/MnO_2 hybrid with a MnO_2 plating time of 20 min. The hybrid nanostructure can be identified by the contrast between the bright MnO_2 filler and the dark gold skeleton. Adapted with permission from Ref. [47]. Copyright (2011) Nature Publishing Group. (For interpretation of the references to colour in this figure legend, the reader is referred to the web version of this article.)

Please cite this article in press as: J. Cao, et al., Journal of Power Sources (2015), http://dx.doi.org/10.1016/j.jpowsour.2015.05.115

3.2. Metal oxides and nitrides

The critical requirement for the metal oxides/nitrides as candidates of electrode scaffold materials is the electrical conductivity. Table 3 lists the typical electrical conductivities of the potential metal oxides/nitrides for fabrication of electrode scaffolds.

3.2.1. ZnO

ZnO has better electrical conductivity (10^2–10^3 S cm^{-1}) [105] than MnO_2, and is both chemically and electrochemically stable in neutral aqueous electrolyte within the working potential window of MnO_2 electrodes [62]. Thus ordered ZnO nanorod/wire arrays have been widely used for fabrication of ZnO–MnO_2 core–shell hybrid arrays [62,106–112]. Methods including electrodeposition [62,108,110], seeds assisted chemical bath [107,111] and hydrothermal methods [109,112,113] were used to grow ZnO arrays on either flat conductive substrate (metal sheets [62,106] and FTO/ITO glass [108,110]) or on flexible carbon cloth [107,109,111,112].

3.2.2. TiO_2

TiO_2 suffers from poor electrical conductivity (10^{-5}–10^{-2} S cm^{-1}) [114] and low electrochemical activity, which lead to small reported specific capacitances (below 0.1 mF cm^{-2}) of the anodized TiO_2 nanotube arrays [115,116], and poor rate capability of TiO_2 nanoblet-MnO_2 core–shell arrays electrode [117]. Nevertheless, hydrogenated TiO_2 (H–TiO_2) nanostructures have been reported to be suitable scaffolds for loading MnO_2 due to the increased carrier density and electrochemical activity [29,64].

3.2.3. TiN

TiN has high electrical conductivity (10^4–10^6 S cm^{-1}) [118] and superior chemical resistance to acids/alkali medium [118,119]. Nanostructured TiN materials with high surface area have already been investigated as double layer capacitance materials for supercapacitor application [118–120]. TiN nanotube arrays fabricated by nitriding of anodized TiO_2 nanotube arrays at high temperature under ammonia atmosphere [61,119,121,122] or by template assisted atomic layer deposition [123], exhibited great potential in fabrication of high performance MnO_2 electrodes with remarkable rate capability [61,121–123]. Besides, the nitrided film of layer assembled hollow TiO_2 shells has also been demonstrated to be an excellent scaffold to support pseudo-capacitive materials [124].

3.2.4. Co_3O_4 and $NiCo_2O_4$

Co_3O_4 is a good pseudo-capacitive material having better electrical conductivity (0.005–1.5 S cm^{-1}) [125] than MnO_2. Fan et al. designed and fabricated a hybrid Co_3O_4–MnO_2 core–shell nanowire arrays with both core and shell materials are good pseudo-capacitive materials (Fig. 6) [63]. As shown in Fig. 6a, the MnO_2 nanosheets shell reacts with Li^+ cations in the 1 M LiOH electrolyte, while the Co_3O_4 nanowire core reacts with OH^- anions during charging/discharging process *via* [126]:

$$Co_3O_4 + OH^- + H_2O \leftrightarrow 3CoOOH + e^- \quad (4)$$

$$CoOOH + OH^- \leftrightarrow CoO_2 + H_2O + e^- \quad (5)$$

As a result, the hybrid system led to an area normalized capacitance of 0.56 F cm^{-2}, which is over 4 times larger than that of the pristine Co_3O_4 nanowire array [63].

Generally, for fabrication of Co_3O_4 nanostructures, $Co(OH)_2$ precursors were firstly synthesized by hydrothermal [63,127,128] or electrochemical [129] method, and then transformed to Co_3O_4 arrays by thermal annealing. In some cases, a conductive layer (such as Au [129] and PPy [127]) was coated on the surface of Co_3O_4 arrays before MnO_2 loading to enhance the electron transfer of the electrodes.

Ternary $NiCo_2O_4$ possesses much better electrical conductivity (1.5–200 S cm^{-1}) [125] when compared to Co_3O_4. $NiCo_2O_4$ nanowires arrays grown on Ni foam *via* two-step hydrothermal-annealing method have been used as scaffold for loading MnO_2 [130,131]. Excellent areal capacitance of 3.31 F cm^{-2} was achieved thanks to the synergic pseudo-capacitive energy storage mechanism of both MnO_2 and $NiCo_2O_4$ [130].

Many other metal oxides with good conductivity, including SnO_2 [42,132], Zn_2SnO_4 [43], ITO [133,134] and WO_{3-x} [135], have also been explored as electrode scaffold materials for fabrication of MnO_2 electrodes. Nanowire arrays of these metal oxides have been successfully grown on metal [42,132–134] or carbon fabric [43,135] substrates *via* vapour transport [42,43,133–135] or template assisted atomic layer deposition [132] methods.

Table 3
Typical electrical conductivities of some metal oxides/nitrides.

Materials	Conductivity/S cm^{-1}	Ref.
MnO_2	10^{-6} to 10^{-3}	[32]
TiO_2	10^{-5} to10^{-2}	[114]
V_2O_5	10^{-4} to 10^{-2}	[9]
NiO	0.01 to 0.32	[9]
Co_3O_4	0.005–1.5	[122,245]
$NiCo_2O_4$	1.5 to 200	[125]
$W_{18}O_{49}$	4 to 11	[256]
SnO_2	5 to 74	[42]
ZnO	10^2 to 10^3	[105]
ITO	2×10^3	[257]
Zn_2SnO_4	10^2 to 10^3	[43]
RuO_2	1 to 10^4	[258]
TiN	10^4 to 10^6	[118]
VN	1.6×10^6	[259]

3.3. Carbon materials

The family of carbon materials is widely used in the electrochemical industry because of the outstanding chemical and physical properties, such as high electrical conductivity, chemical stability in both acidic and alkaline medium, low density, and most importantly, variety in structure (fullerene, CNTs, graphene, activated carbon, carbon fibres, etc.). These features enable carbon materials to be the most popular scaffold materials for fabrication of MnO_2 electrodes. In most cases, these nanostructured carbon scaffolds with high surface area are good double layer capacitance electrodes themselves.

3.3.1. CNTs

CNTs have superior electronic conductivity and outstanding mechanical property. CNTs can be synthesized or processed into various macro-scale forms which act as high surface area electrode scaffolds for further loading MnO_2. Briefly, CNTs scaffolds can be classified into three categories: (1) vertically aligned CNTs arrays; (2) supported CNTs films/coatings; (3) free standing CNTs assemblies.

3.3.1.1. Vertically-aligned CNTs arrays. Successfully synthesis of CNTs arrays on bulk metal have been reported in 2006 [136]. Double layer capacitor constructed by the Inconel-CNTs electrode exhibited outstanding high rate performance. Until now, vertically-aligned CNTs arrays have been successfully grown on various conductive substrates, including flat Ta foil [45], graphite plate [137], Si wafer [138] and textile carbon cloth substrate [75,139]. In

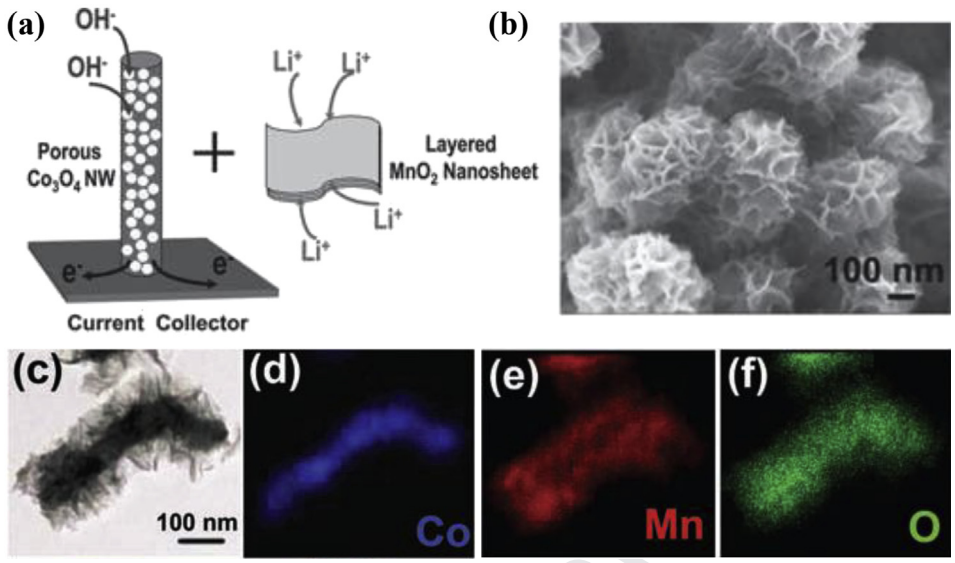

Fig. 6. (a) Schematic of the charge storage advantage of the hybrid nanowire array, in which both the Co_3O_4 core and MnO_2 shell contribute to the charge storage. (b) Typical SEM image of the hybrid array after 5000 cycles. c–f) EDS mapping results from a single hybrid nanowire, demonstrating the Co_3O_4 core/MnO_2 shell hierarchical structure. Adapted with permission from Ref. [63]. Copyright (2011) WILEY-VCH Verlag GmbH & Co. KGaA, Weinheim.

addition to the directly grown CNTs arrays, MnO_2/carbon tube hybrid arrays fabricated by template assisted methods have been reported as supercapacitor electrodes [140,141].

For practical use, large scale production of dense and long vertically-aligned CNTs arrays at low cost is highly required. Zhang el al. electrodeposited MnO_2 nanoflowers on vertically-aligned CNTs arrays (CNTA) framework (35 μm in thickness), the CNTA framework provide superior electronic conductive path and ion diffusion route. As a result, the binder-free electrode with a MnO_2 mass loading of 5 mg cm^{-2} presents a gravimetric capacitance of 199 F g^{-1} (based on the total mass of CNTs and MnO_2) and volumetric capacitance (305 F cm^{-3}) with excellent rate capability (50.8% capacity retention at 77 A g^{-1}), and together with a long cycle life [45].

3.3.1.2. Supported CNTs films. Entangled porous CNTs films supported by conductive substrate (such as ITO glass, stainless steel, etc.) could provide good electron and ion transfer routes. Several methods have been used to prepare CNTs film on conductive substrate, including CVD [142,143], electrophoretic deposition [88,144], layer by layer assembly [145] and electrostatic spray deposition [146].

3.3.1.3. Free-standing CNTs assemblies. Free-standing CNTs assemblies, such as CNTs paper [87,147,148] and CNTs sponge [82], are light in weight, electrical conductive, porous and flexible. CNTs papers were generally prepared by vacuum filtration of CNTs dispersions [87,147,148]. Filtration of single- or double-walled CNTs dispersion resulted in densely packed CNTs paper, and further led to inhomogeneous deposition of MnO_2 along the cross section of the CNTs paper [87,147]. Large scale and mechanical robust CNTs papers with sufficient porosity and excellent electrical conductivity (4350 S cm^{-1}) could be achieved by using multi-walled CNTs with increased length (several micrometers) and diameter (50–80 nm) [148].

3.3.2. Graphene

As the building block of any other carbon material, two dimensional (2D) graphene has attracted great research attentions since it was first reported in 2004 [149]. Monolayer graphene sheet can possess extraordinary physical and chemical properties, such as high electronic conductivity, high specific surface area, and is a competitive (though relatively expensive) candidate for building electrode architectures [150–152].

Chemically converted graphenes (CCGs), including graphene oxide (GO) and reduced graphene oxide (rGO), are ideal building blocks for "bottom-up" nanotechnology thanks to its molecular behaviour [153]. Various macroscopic architectures have been fabricated by using GO or rGO as building blocks, including 1D graphene fibre [154–157], 2D graphene paper/film [158–161], and 3D graphene hydrogel/aerogel [81,162]. This has motivated great research efforts to use these CCGs macroscopic architectures as scaffolds for loading MnO_2 active phase [156–159,162,163]. However, for the graphene fibres and papers, the compact restack of rGO sheets after assembly cannot allow a homogenous incorporation of MnO_2 into the fibre or paper structures [156–159]. MnO_2 was generally deposited on the surface of the fibres or papers [156–159]. *In-situ* incorporation of MnO_2 during the fabrication process of the macroscopic CCGs assemblies is an effective strategy to achieve uniform distribution of MnO_2 active phase [89,161].

Recently, Cheng et al. synthesized a 3D graphene (3DG) network by nickel foam templated CVD growth [164]. The robust, conductive and porous 3DG network inspired series works about using it as scaffold for loading MnO_2 [66,165,166]. A large MnO_2 loading of 9.8 mg cm^{-2}, which is about 92.9 wt.% of the entire electrode, has achieved with the 3DG network scaffold [66], the increased mass portion of active MnO_2 in the electrode is benefit for the specific capacitance normalized by the total weight of the entire electrode.

3.3.3. Carbon fibres

In most cases, carbon fibres are produced by carbonization/graphitization of polymer fibres which are synthesized by spinning. Depending on the diameter, carbon fibres can be classified as carbon microfibres (CMFs) and carbon nanofibres (CNFs). The simplicity and versatility of electrospinning in fabrication of ultrathin nanofibres from various precursors have attracted considerable research attention [167].

Commercial CMFs with a diameter range of 5–10 μm are

produced by industrial scale spinning. CMFs can be further processed into various textures, such as cloths and papers. The low cost, commercial available, mechanical stable and highly conductive CMFs based fabrics are ideal scaffold for fabrication of flexible and light weight MnO_2 based electrodes [29,43,84,107,112,135,168–171].

Single phase MnO_2 with various nanostructures have been directly grown on the surface of CMFs, such as nanosheets arrays [168,172], well-ordered whisker-like arrays [173], nanorods arrays [170], worm-like amorphous nanowires [171] and nanoflowers [79]. However, the micrometers scale CMFs lack of enough surface area, which leads to thick MnO_2 active layer thus poor MnO_2 utilization in most cases. An effective strategy is to build secondary nanostructures on the surface of CMFs sub-scaffold.

CNFs with diameters from several tens to few hundreds of nanometers will undoubtedly provide more specific surface area for loading active material when compared with CMFs. Free standing CNFs networks could not only provide high surface area conductive scaffolds for MnO_2 loading, but also fast ion transfer routes by the interconnected pores. These merits have motivated series research about using CNFs networks as nanostructured current collectors for loading MnO_2 active phase [28,65,78,174,175].

In most cases, the free-standing CNFs networks were synthesized by electrostatic spinning, followed by hot-pressing and high temperature carbonization [65,78,174,175]. Such electrospun CNFs have a diameter from 50 to 250 nm and length up to hundreds of microns [65]. Relatively good conductivities around 10 S cm^{-1} were reported for these electron spun CNFs networks [174,175], and the conductivity could be further improved to 24.1 S cm^{-1} by incorporation of CNTs into the polyaniline precursor solution (CNTs embedded CNFs) [174].

In addition to electrospun CNFs networks, a bacterial-cellulose-derived ultrafine CNFs (10–20 nm in diameter) network has also been reported as a good MnO_2 loading scaffold [28]. CVD grown vertically aligned CNFs arrays have already been investigated for loading MnO_2 earlier in 2010 [176].

Besides CNTs, graphene and carbon fibres, carbon nanowalls (also called graphitic petals) grown by CVD methods and flexible carbon foam synthesized by simple carbonization of commercial melamine resin foam were also employed for loading MnO_2 active phase [86,177–179].

3.3.4. Binary carbon scaffolds

Mono carbon material based scaffolds usually suffer from drawback of small MnO_2 loading mass due to either the intrinsic low specific surface area (carbon cloth) or aggregation/restack after being fabricated into macroscopic architectures (CNTs or graphene paper/film). In this consideration, various binary carbon/carbon composite scaffolds have been developed to improve the loading surface area. Moreover, incorporation of secondary carbon component into the primary carbon skeleton could also improve the electrical conductivity [174] and mechanical robustness [89] in some cases.

Building secondary carbon nanostructures on the electrical conductive and mechanical robust CMFs fabrics backbones are the mostly researched tactic to fabricate binary carbon/carbon nanostructured current collector. Long's group fabricated a carbon nanofoam paper with periodic submicrometer pore networks interconnected in 3D by pyrolysis of a polymer-filled commercial carbon fibre paper [46]. As shown in Fig. 7, the carbon nanofoam paper can be scaled not only in the x-y direction but also in the z direction by stacking multiple layers (one ply, two ply and three ply corresponding to the stacking of one, two and three layers, respectively) of sol-infiltrated carbon papers while maintains the uniform nanofoam nature. The carbon nanofoam paper exhibits an areal capacitance of 7.5 F cm^{-2} (three ply) after loading of 10 nm thick MnO_x deposits all through the thickness (230 μm) of carbon nanofoam paper. The uniform deposition of nanoscale MnO_2 without deterioration of nanoporosity of the carbon paper is the key to the excellent capacitance behaviour.

In addition to the carbon nanofoam paper [44,46,180], including CNTs coatings [181], aligned CNTs arrays [75,139], and carbon nanoparticles [84] have been built on the CMFs fabric backbones and act as high surface area scaffolds for loading MnO_2 active phase. Recently, CNTs and CNFs forests have been successfully grown on the surface of 3D graphene networks to further enhance to the loading surface area [182–184].

The problem of restack/aggregation of graphene/CNTs in graphene/CNTs films/coatings can be solved by incorporation of secondary carbon component with different dimensions. Such as incorporation of zero dimensional (0D) carbon nanoonions into 1D CNTs assembled films [185], as well as 0D carbon black or 1D CNTs into 2D graphene sheets assembled films/coatings [174,186,187]. The secondary carbon components act not only as spacers to prevent the graphene/CNTs form restack/aggregation, but also as conductive/mechanical reinforcement to provide interlinked electron pathways. For example, flexible graphene/MnO_2/CNTs composite film paper was fabricated by filtration of a mixed dispersion of MnO_2 coated graphene and CNTs (Fig. 8). As shown in Fig. 8b, MnO_2 was homogenously incorporated into the composite paper. The interconnected CNTs act as electron conductive pathway and mechanical reinforcement in the composite paper. As a result, the as-fabricated mechanical robust (48 MPa in tensile strength, Fig. 8c) graphene/MnO_2/CNTs composite paper with a MnO_2 loading of 56 wt.% exhibits a specific capacitance of 326 F g^{-1} (based on the total mass of the composite paper) with good rate capability and cycling stability [89].

3.4. Conducting polymers

Conductive polymers are another category of pseudo-capacitive materials besides metal oxides [4,8]. Polyaniline (PANI), polypyrrole (PPy), polythiophene (PTh) and their derivatives (such as PEDOT) are the most widely researched pseudo-capacitive conductive polymers [10]. Conductive polymers have intrinsic high electrical conductivity in doped state and exhibit plastic properties and are readily produced as thin films [10].

Conductive polymers are normally used to form ternary core-double-shell hybrid structures, where conductive polymer acts either as intermediate or outer shell [78,79,82,110,127,139,169,188–190]. Besides enhancing the electrical conductivity of the electrodes and providing pseudo-capacitance, the intermediate conductive polymer shell could also act as sacrificing material for conformal *in-situ* deposition of MnO_2 [78,82,110,127], while the conductive polymer outer layer could protect the MnO_2 active phase from dissolution in acidic gel electrolyte [79,169]. Thanks to its excellent electrical conductivity, chemical stability and good mechanical flexibility, PEDOT has also been directly employed as a scaffold material [67–69,190,191].

3.5. Natural cellulose and synthetic fibres

Textile, sponge and paper, which are made of natural cellulose or synthetic fibres, are highly flexible, mechanical robust and low cost. Although these natural cellulose or synthetic fibres are not intrinsically electrical conductors, the hierarchically structured and superior hydrophilic surface makes these fibres can be strongly coated with highly conductive CNTs or graphene sheets *via* van der Waals forces and hydrogen bonding by a simple solution based coating method [48]. Thus, these conductively modified flexible

Please cite this article in press as: J. Cao, et al., Journal of Power Sources (2015), http://dx.doi.org/10.1016/j.jpowsour.2015.05.115

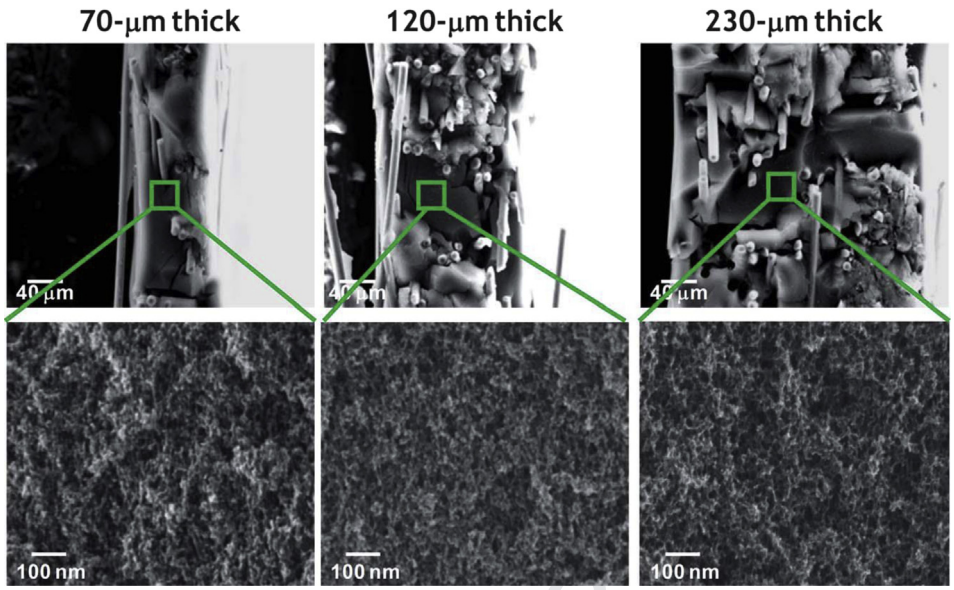

Fig. 7. SEM images of cross-sectioned one-ply, two-ply, and three-ply (from left to right) carbon nanofoam papers at low and high magnifications. The images demonstrate the high quality and uniform nature of the nanofoam fill within a single layer of 70 μm thick carbon paper (one ply) or throughout two- and three-layer thick composites. Adapted with permission from Ref. [46]. Copyright (2011) Royal Society of Chemistry.

textiles, sponges and papers have been widely investigated as electrode scaffolds for loading active pseudo-capacitive materials [48,50,73,74,188,192–197]. Cui's group conducted pioneer work on the solution based conductive coating of textiles with CNTs or graphene ink [48,73,188,192]. The CNTs coated textile shows a conductivity of 125 S cm^{-1} and delivers an areal capacitance of 0.45 F cm^{-2} after MnO_2 loading [48].

4. Deposition of MnO_2 on electrode scaffolds

Deposition of nanoscale MnO_2 active phase on the electrode scaffolds without blocking the ion diffusion tunnels

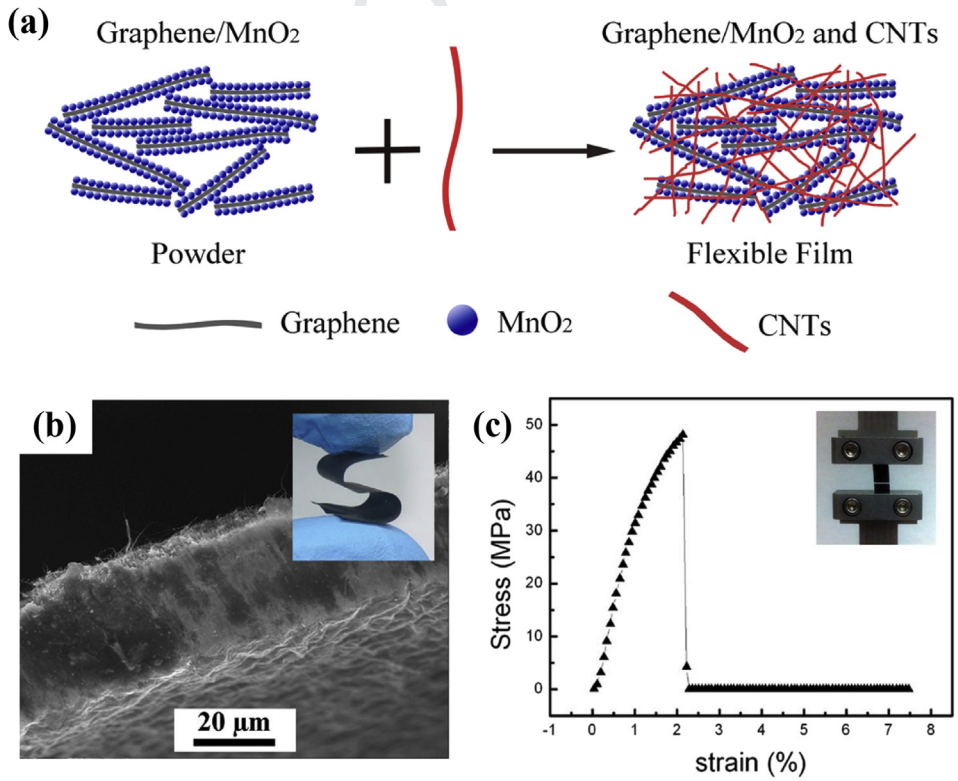

Fig. 8. (a) Schematic illustration of the fabricated flexible and conductive film using graphene/MnO_2/CNTs. Note the difference in the possible electron paths for the two architectures: electron has to pass the insulating MnO_2 layers for the graphene/MnO_2 composite (left) while the interconnected CNTs provide rapid electron conductance for the flexible film shown on the right. (b) Cross-sectional SEM image and a picture of the (inserted at the top right corner) of film showing the flexibility of these structures. (c) Typical stress–strain curve for the graphene/MnO_2/CNT composite film with 25 wt.% of CNTs. Adapted with permission from Ref. [89]. Copyright (2012) American Chemical Society.

Please cite this article in press as: J. Cao, et al., Journal of Power Sources (2015), http://dx.doi.org/10.1016/j.jpowsour.2015.05.115

(interconnected pore structures) is the key procedure to achieve good pseudo-capacitance. The most popular deposition methods are electrochemical deposition and *in-situ* redox deposition.

4.1. Electrochemical deposition

Electrochemical deposition is probably the earliest and most versatile method that used to prepare manganese oxide film on conductive substrate. Electrodeposition of MnO_2 involves the oxidation of Mn^{2+}, reduction of Mn^{7+}, or oxidation of low valent Mn metal or oxides (such as Mn_2O_3 and MnOOH). Based on the basic electrochemical principals, the electrochemical deposition of MnO_2 can be simply classified as anodic electrodeposition and cathodic electrodeposition.

4.1.1. Anodic electrodeposition

Known as electrolytic manganese dioxide (EMD), anodically deposited MnO_2 from acidic Mn^{2+} solutions have been widely used in the battery industry for a very long time [198,199]. Pang et al. first studied the pseudo-capacitive performances of anodic deposited MnO_2 thin film in 2000 [17,200]. This work has motivated diverse interests in using anodic deposited MnO_2 thin films as supercapacitor electrodes. The earliest studies mainly focused on deposition of MnO_2 thin film with various water contents, oxidation states and specific surface areas by adjusting the deposition parameters [35,201–210]. However, despite great efforts have been devoted in optimization of the deposition parameters, these as-deposited continuous MnO_2 coatings on planar current collectors lack both electron and ion transport pathways, thus only could deliver small capacitances because of poor MnO_2 utilization [204,205,210,211]. Later, attentions transferred to morphology controlled growth of single-phase MnO_2 nanostructures, because of the interconnected macro/meso pores provided by the nanostructured MnO_2 deposits could act as fast ion diffusion routes. MnO_2 deposits with various nanostructures have been synthesized by morphology controlled anodic deposition with or without template assistance, such as nanorods [38], nanowires [33,37,171,212–215], nanotubes [37], interconnected nanosheets [27,216,217] and macroporous film [218,219]. Recently, with the development of architecture-designed electrode scaffolds, anodic electrodeposition have been widely employed to deposit nanoscale MnO_2 on the electrode scaffolds, including metal oxide/nitride nano-array scaffolds [29,61,92,121,122,129,130,134,135,220], metal/carbon nanostructured current collectors [45,66,90,91,93,121,137,142,143,146,148,176,182] and flexible textile/paper/fibre scaffolds [48,50,73,74,168,169,188,192,197].

The anodic electrodeposition of MnO_2 from manganous ions in neutral or acidic solutions can be written as:

$$Mn^{2+} + 2H_2O \rightarrow MnO_2 + 4H^+ + 2e^- \quad (6)$$

Although the underlying mechanism is complicated, the well-accepted anodic formation mechanisms for pure MnO_2 occur *via* two pathways, depending on the acid concentration of the deposition solution, detailed discussions about the mechanisms are available in the earlier papers [221–224].

Anodic deposition of MnO_2 can be realized by several electrical modes, including potentiostatic, galvanostatic, potentiodynamic (linear sweep voltammetry and cyclic voltammetry), and pulse potential/current modes. Factors such as deposition potential, current density, passed charge, pH value, Mn^{2+} concentration, anion type, deposition temperature and additives have significant influences on the MnO_2 deposition. It is clear that the passed charge directly links to the thickness and mass of the MnO_2 deposits [35,225], and the passed charge depends on the current density and deposition time, while the former has a close relationship with deposition potential. The deposition potential decides whether the deposition is carried out *via* electron or mass transfer controlled condition, and further influences the structure and oxidation states of the deposits [203]. On the other hand, the current density is correlated to the nucleation and growth rate of the MnO_2 deposits, thus have significant influences on the morphologies of the MnO_2 deposits [216,223]. Almost all the influences of any other factors on the MnO_2 deposition could be reflected by the changes of deposition potential and current density.

By understanding the influences of deposition parameters on the morphology evolution of MnO_2 deposits, MnO_2 with various nanostructures could be synthesized without any assist of template [27,38,171,216,226,227]. Wei et al. ascribed the influences of deposition parameters on the evolution of MnO_2 morphology to the supersaturation ratio of electrolyte components (Mn^{2+} and OH^- for MnO_2 anodic deposition) at the electrode/electrolyte interface [216]. Adjusting the deposition parameters, including Mn^{2+} concentration, overpotential (current density), solution pH and temperature, would directly change supersaturation ratio and thus the kinetics of electrodeposition process. With the decrease of supersaturation ratio, the electrodeposition process changes from high nucleation rate to epitaxial growth, leading to the evolution of MnO_2 morphologies from continuous coating to interconnected nanosheets [216]. On the other hand, filling the template membranes is another effective way to achieve highly ordered/periodic MnO_2 nanostructures through anodic electrodeposition. Templates as anodic Al oxide (AAO) [33,37,214,215,228] and polystyrene spheres [218,219] are widely used to synthesize ordered MnO_2 nanowire arrays and macoporous MnO_2 nanostructures, respectively.

For anodic electrodeposition of nanoscale MnO_2 on the electrode scaffolds, particular considerations must be paid to achieve uniform MnO_2 deposits all through the thickness of the electrode scaffolds. Generally:

(a) Pretreatments are needed for some scaffolds, such as hydrophilic treatment for some carbon based scaffold by CV cycling in acidic electrolyte [182]; plating electrolyte impregnation by vacuum infiltration for some large aspect ratio array scaffolds (CNTs arrays, Ni nanorods arrays etc.) [45,75,93].
(b) Relatively less positive potentials (0.4–1 V) are preferred under potentiostatic mode, as at which electron transfer rather than mass transfer controlled nucleation and growth occurs [61,90,93,121].
(c) Under galvanostatic mode, small deposition current densities (0.2–1 mA cm^{-2}) are chosen to assure a low overpotential and slow growth rate for uniform deposition [75,129,131,135].
(d) Pulse deposition technics, including pulse potential [60,93,146] and current [66,182] methods, are effective to avoid mass transfer controlled reaction due to the depletion of Mn^{2+} inside the scaffolds, thus giving uniform MnO_2 deposits all through the scaffold thickness.

In real situations, factors like scaffold materials and architectures, Mn^{2+} concentrations, electrolyte additives, deposition temperatures etc. all have impacts on the deposition of MnO_2 on the electrode scaffolds. It is difficult to give a definitive statement about optimum deposition conditions. Nevertheless, a pre-performed LSV scan could effectively help the researchers to choose appropriate deposition parameters (potential, current density) under particular conditions [208,224,225].

4.1.2. Cathodic electrodeposition

In most cases, cathodic deposition involves electro-reduction of Mn(VII) to MnO_2 deposits on the cathode surface as:

$$MnO_4^- + 2H_2O + 3e^- \rightarrow MnO_2 + 4OH^- \quad (7)$$

Typically, this reaction produces a birnessite-type manganese oxide (A_xMnO_2) thin film with morphology of wrinkled thin sheets [229,230]. This cathodic deposition approach has been used to load MnO_2 on CNTs arrays grown on stainless steel mesh [142].

Another cathodic deposition of MnO_2 involves formation of manganese hydroxide precursors on the cathode surface in Mn(II) solutions as:

$$Mn^{2+} + 2(OH)^- \rightarrow Mn(OH)_2\downarrow \quad (8)$$

This is due to the increased local pH value caused by consuming of H^+ or electrolysis of water on the surface of the cathode. After subsequent thermal annealing, the manganese hydroxide will convert to stable manganese oxides [11,231]. A potential pulse cathodic electrodeposition has been employed to coat a uniform manganese oxides (mixture of MnO_2 and Mn_3O_4) shell on vertically aligned CNFs arrays [176]. A so-called electrochemically induced deposition method was used to deposit highly dispersed MnO_2 on well-aligned CNTs arrays, which served as cathode during the deposition process [137].

In some studies, metallic Mn instead of $Mn(OH)_2$ was deposited by cathodic electrodeposition as:

$$Mn^{2+} + 2e^- \rightarrow Mn\ (Electro-reduction) \quad (9)$$

The subsequent air annealing or anodic oxidation of Mn metal could give a uniform MnO_2 deposits [59,62,85]. Since metallic Mn has much better electrical conductivity than MnO_2, the cathodic electrodeposited Mn nanostructures have been used to fabricate Mn/MnO_2 core–shell hybrid electrodes [59,85].

4.2. In-situ redox deposition

In-situ redox deposition of MnO_2 onto carbon substrates was firstly reported by Chen and co-workers in 2004 *via* immersing a graphite disk electrode in acidic solution of $KMnO_4$, where redox reaction between MnO_4^- and carbon occurred and MnO_2 deposited on the carbon surface [232]. This *in-situ* redox deposition process is simple and scalable for preparation of MnO_2/carbon composites, thus immediately attracts research attentions [76,233–243]. However, the earlier studies are mostly focused on synthesis of powder composite materials *via* the reduction of MnO_4^- ions in aqueous dispersions of carbon nanomaterials, such as acetylene black [235,236,240], templated mesoporous carbon [233,234,241,243], CNTs [237–240,242], and graphene [76].

The MnO_2-carbon nanofoam paper electrodes were developed by Long's group in 2007 by incorporation of homogeneous nanoscale MnO_2 within ultraporous carbon nanofoam paper *via in-situ* redox deposition [44,46,244]. This has motivated numerous research interests concerning *in-situ* deposition of nanoscale MnO_2 within and onto nanostructured carbon scaffolds, including CNTs films [87,144,145,181], graphene foam [174], graphene fibre [157], 3D macroporous graphene frameworks [245], CMFs [49,172,173,246], CNFs papers [28,65,174,175,247], CNFs forests [183], etc. Recently, *in-situ* redox deposition of MnO_2 was further extended to metal oxides nanostructures by reaction between MnO_4^- and a pre-painted carbon coating on the metal oxides surface [63,106,107,117,248]. *In-situ* redox deposition could also be realized by redox reactions between MnO_4^- and conducting polymer nanostructures [68], so this could be further extended to conducting polymer coated carbon [78,82] and metal oxides [110,127] scaffolds.

In a neutral pH solution, the *in-situ* redox reaction between MnO_4^- precursor and carbon substrate occurs as [236]:

$$4MnO_4^- + 3C + 2H_2O \rightarrow 4MnO_2 + 3CO_2 + 4OH^- \quad (10)$$

The CO_2 could either evolve or be absorbed by OH^- and then transform to CO_3^{2-} and HCO_3^- species, depending on the reaction and absorption rate [236]. Another well-accepted reaction equation for mild redox reaction between MnO_4^- and carbon in a neutral solution is [237]:

$$4MnO_4^- + 3C + H_2O \rightarrow 4MnO_2 + CO_3^{2-} + 2HCO_3^- \quad (11)$$

In acidic solution, fast gas bubbling (CO_2) could be observed when adding graphite powder into the deposition solution, as reported by Chen and colleagues [232].

A nanoscale micro-electrochemical cell reaction model was proposed by Chen et al. [232], in which the carbon oxidation occurs at the anode region (characterized by carbon defects and edge planes) while the MnO_2 growth at the cathode region (near the defect site). Electrons transfer from the anode to the cathode through the carbon substrate and pre-formed MnO_2 deposits. This model could well explain the growth of MnO_2 on the smooth surface and inside the CNTs [232], and could also help understanding the completely conversion of CNFs to fibre-like structures assembled by MnO_2 nanosheets after a sufficiently long reaction time (168 h) [247].

Nevertheless, once most of the carbon surface is covered with MnO_2, the redox reaction between MnO_4^- and carbon is inhibited and slow down to a low rate [243]. If the reaction occurs at elevated temperature (hydrothermal condition) and/or acidic solution, the self-decomposition of MnO_4^- according to [249,250]:

$$4MnO_4^- + 2H_2O \rightarrow 4MnO_2 + OH^- + 3O_2 \quad (12)$$

would be the dominant reaction, and lead to the deposition and growth of MnO_2 nanostructures on the preformed MnO_2 deposits which serve as nucleation sites [250,251]. Moreover, the nucleation and growth of MnO_2 nanostructures through the self-decomposition of MnO_4^- are sensitive to pH and permanganate concentration [165,173,249], thus could be used to tune morphologies of the as-formed MnO_2 nanostructures.

The redox reaction between permanganate and carbon is influenced by various experimental parameters, such as pH, temperature, functionality of the carbon surfaces, permanganate concentration, etc.

(1) pH (acidic to neutral): The reduction reaction between MnO_4^- ions and carbon could be accelerated by acidic solutions [238]. However, the competing reaction of autocatalytic decomposition of permanganate could be also enhanced by acidic conditions [44], which would roughen the MnO_2 morphology [238] or even leading to inhomogeneous deposition of MnO_2 [44]. Self-limiting deposition carried out at neutral pH condition and room temperature could give a homogeneous nanoscale MnO_2 deposits on various nanostructured carbon scaffolds [28,44,46,145,244,245], even within carbon nanofoam paper which has pore sizes between 10 and 60 nm and thickness up to 170 μm [44,244].

(2) Temperature: Ma et al. reported that the reduction time can be dramatically shortened by increasing the temperature, and the reaction rates almost doubled for every 10 °C rise in temperature [235]. Methods like conventional heating [86,175,246], and microwave irradiation [76,183,239] were

used to accelerate the reaction in some cases. However, once the temperature is elevated to reach certain level (normally under hydrothermal conditions), the self-decomposition of permanganate becomes dominate, and leads to further deposition and growth of MnO_2 nanostructures. This hydrothermal deposition method was used to grow MnO_2 nanostructures on the carbon cloth [172,173], graphene foam [165], and carbon-painted metal oxides arrays substrates [63,117,248], which possess macro-porous structures, thus could afford relatively thick MnO_2 deposits without block the ion diffusion channels.

Besides, carbon surface rich with defects, such as edge planes, carbonyl, carboxyl, and hydroxyl groups, are more vulnerable to be oxidized than defect-free graphene surface [237]. Permanganate concentration and reaction time were generally used as parameters to control the MnO_2 uptake (loading mass) [183,244].

However, despite the advantages of simplicity and scalability, a recent study about *in-situ* redox deposition of MnO_2 onto reduced graphene oxide indicated that the carbon-destructive reaction between MnO_4^- and carbon results in not only carbon consumption but also the deterioration in electrical conductivity of the remain carbon due to the disrupted π-conjugated carbon network [252]. Therefore, particular consideration should be paid before employing the *in-situ* redox deposition method, especially for the carbon scaffold assembled by graphene, single-walled CNTs and few-walled CNTs. An effective way to avoid the corrosion of carbon scaffolds is to coat a sacrificing conducting polymer layer before MnO_2 deposition [82].

For *in-situ* redox deposition of MnO_2 on PEDOT nanowire arrays, possible reaction mechanisms proposed by Liu et al. was the oxidation of thiophene sulfur into sulfoxide by $KMnO_4$, along with the reduction of permanganate to MnO_2 [68]. Similar reaction might also be used to explain the redox reaction between PPy and $KMnO_4$.

MnO_2 could also be deposited on SnO_2 [42] and Zn_2SnO_4 [43] nanowire arrays without carbon coating under mild conditions in which the self-decomposition of permanganate was suppressed. The proposed mechanism involves direct electron transfer from the electron rich metallic substrate to the permanganate ion through the SnO_2 nanowires [42].

Other methods for deposition of MnO_2 include reduction of permanganate with Mn^{2+} [39], N_2H_4 vapour [47], ethanol [124,253,254], polyethylene glycol [184]; oxidation of Mn^{2+} with H_2O_2 [255], $(NH_4)_2S_2O_8$ [166]; direct decomposition of permanganate under hydrothermal environment without any reductant [128,130].

5. Conclusions and outlook

Recent advances in architecture-designed MnO_2 electrodes have been summarized in this review, including the strategies for electrode architecture design, materials and fabrication of the electrode scaffolds, methods for deposition of MnO_2 within the electrode scaffolds and rational evaluations of the performance of these MnO_2 electrodes. Metal (such as Au, Ni and Mn) and metal oxide (ZnO, TiO_2, TiN and Co_3O_4) based core–shell hybrid nanostructures and nanostructured current collectors could give high specific capacitance approaching the theoretical value and good rate capability, but only with limited MnO_2 mass loading below 1 mg cm^{-2}. 3D carbon scaffolds like vertically aligned CNTs arrays, 3D graphene networks and self-support carbon nanofoam paper, which have the capability to afford large MnO_2 mass loading while maintain good rate capability, have great potential of application in real supercapacitors. The recently rising textile, sponge and paper based electrode scaffolds opened a new way to develop flexible supercapacitors, and incorporation of MnO_2 within/onto these flexible textile/sponge/paper electrodes is a powerful way to enhance their energy storage capacity. All these significant progress are supported by the development of MnO_2 deposition technologies (electrochemical deposition and *in-situ* redox deposition), which assure homogeneous incorporation of MnO_2 within or onto these nanostructured electrode scaffolds.

Nevertheless, great challenges still remain for electrochemists, material scientists and engineers since the performance of most of the reported electrodes/supercapacitors is still far below that of the commercial activated carbon electrode/device if the capacitance and energy densities/power densities are normalized by the total weight or volume of the electrodes/devices. Some possible ways to conquer this challenge and bring the MnO_2 electrodes from laboratory studies to real-world applications are listed below:

(1) Standardized test fixture configurations, measurement procedures and data reporting rules are highly required to rationally evaluate the true performance of the electrodes and the assembled supercapacitors. For example, any reporting of energy density and power density should be based on a packaged two-electrode test configuration and normalized by the total weight/volume of the test device. All the capacitances reported should be deduced from CV or galvanostatic tests in which the charging/discharging time is in the typical time scale of supercapacitors (10^{-1}–10^2 s). As the performance of the MnO_2 electrodes are so sensitive to the MnO_2 mass loading, it is highly recommended that all the information about the electrodes/devices (MnO_2 mass loading, total weight/volume of the electrodes/devices, etc.) should be reported.

(2) Increasing the MnO_2 mass loading to the level of commercial activated carbon electrodes (~10 mg cm^{-2}) while maintaining the high power nature of supercapacitors through developing of electrode scaffolds with large thickness (100–200 μm), high loading surface area, high conductivity and minimized inside dead volume. Most of the present electrode scaffolds cannot afford MnO_2 mass loading higher than 1 mg cm^{-2}, leading to poor areal capacitances. Electrode scaffolds with large thickness, such as hollow nickel dendrite (200 μm), vertically aligned CNTs arrays (35–50 μm), 3D graphene networks (<200 μm) and carbon nanofoam paper (230 μm), have set good examples for developing of electrode scaffolds with high MnO_2 mass loadings. Besides, it is worth pointing out that dead volume of the electrodes, which includes both the excess volume of inert electrode scaffold materials and void spaces, should be minimized when designing electrode architectures for high volume/weight energy density devices.

(3) Boosting the energy density and power density of the MnO_2 based aqueous devices to that of the commercial activated carbon supercapacitors by incorporating the high capacitance and high rate MnO_2 electrodes into high voltage asymmetric systems. Combining positive MnO_2 electrodes with negative carbon electrodes in neutral aqueous electrolyte leads to high cell voltage up to 2.0 V. The MnO_2 positive electrodes with high capacitance and rate performance could assure high energy storage ability without sacrifice the high power nature of supercapacitors. Cycle life of these asymmetric systems need to be further improved to the level of commercial carbon devices (500,000 cycles). If so, the low-cost, high-safety neutral aqueous MnO_2//carbon asymmetric systems would provide competitive, green

Please cite this article in press as: J. Cao, et al., Journal of Power Sources (2015), http://dx.doi.org/10.1016/j.jpowsour.2015.05.115

alternatives to the current commercial EDLCs using flammable and high cost organic electrolytes.

Acknowledgements

The authors thank Prof. D. Pletcher for the constructive discussion. Partial support from the National NSFC grant nos. 51371071 and 51321061 is gratefully acknowledged. J. Cao is grateful to the China Scholarship Council (No. 201306120133) and the National Scholarship for Postgraduate Students for supporting his visiting research at the University of Southampton.

References

[1] B.E. Conway, Electrochemical Supercapacitors: Scientific Fundamentals and Technological Applications, Plenum Press, New York, 1999.
[2] A. Burke, J. Power Sources 91 (2000) 37–50.
[3] M. Winter, R.J. Brodd, Chem. Rev. 104 (2004) 4245–4269.
[4] P. Simon, Y. Gogotsi, Nat. Mater. 7 (2008) 845–854.
[5] J.R. Miller, A.F. Burke, Electrochem. Soc. Interface 17 (2008) 53–57.
[6] L.L. Zhang, X.S. Zhao, Chem. Soc. Rev. 38 (2009) 2520–2531.
[7] M.B. Sassin, C.N. Chervin, D.R. Rolison, J.W. Long, Acc. Chem. Res. 46 (2013) 1062–1074.
[8] G. Wang, L. Zhang, J. Zhang, Chem. Soc. Rev. 41 (2012) 797–828.
[9] M. Zhi, C. Xiang, J. Li, M. Li, N. Wu, Nanoscale 5 (2013) 72–88.
[10] G.A. Snook, P. Kao, A.S. Best, J. Power Sources 196 (2011) 1–12.
[11] W. Wei, X. Cui, W. Chen, D.G. Ivey, Chem. Soc. Rev. 40 (2011) 1697–1721.
[12] T.T. Liu, G.J. Shao, M.T. Ji, Z.P. Ma, Asian J. Chem. 25 (2013) 7065–7070.
[13] C.J. Xu, F.Y. Kang, B.H. Li, H.D. Du, J. Mater. Res. 25 (2010) 1421–1432.
[14] M. Toupin, T. Brousse, D. Belanger, Chem. Mater. 16 (2004) 3184–3190.
[15] H.Y. Lee, J.B. Goodenough, J. Solid State Chem. 144 (1999) 220–223.
[16] H.Y. Lee, V. Manivannan, J.B. Goodenough, C.R. Acad. Sci. Ser. IIc: Chim. 2 (1999) 565–577.
[17] S.C. Pang, M.A. Anderson, T.W. Chapman, J. Electrochem. Soc. 147 (2000) 444–450.
[18] P. Guillemet, T. Brousse, O. Crosnier, Y. Dandeville, L. Athouel, Y. Scudeller, Electrochim. Acta 67 (2012) 41–49.
[19] V. Khomenko, E. Raymundo-Piñero, F. Béguin, J. Power Sources 153 (2006) 183–190.
[20] T. Brousse, P.-L. Taberna, O. Crosnier, R. Dugas, P. Guillemet, Y. Scudeller, Y. Zhou, F. Favier, D. Bélanger, P. Simon, J. Power Sources 173 (2007) 633–641.
[21] L. Demarconnay, E. Raymundo-Piñero, F. Béguin, J. Power Sources 196 (2011) 580–586.
[22] J.Y. Cao, Y.M. Wang, Y. Zhou, J.H. Ouyang, D.C. Jia, L.X. Guo, J. Electroanal. Chem. 689 (2013) 201–206.
[23] M.S. Hong, S.H. Lee, S.W. Kim, Electrochem. Solid-State Lett. 5 (2002) A227.
[24] T. Brousse, M. Toupin, D. Belanger, J. Electrochem. Soc. 151 (2004) A614.
[25] F. Wang, S. Xiao, Y. Hou, C. Hu, L. Liu, Y. Wu, RSC Adv. 3 (2013) 13059.
[26] Z. Fan, J. Yan, T. Wei, L. Zhi, G. Ning, T. Li, F. Wei, Adv. Funct. Mater. 21 (2011) 2366–2375.
[27] H. Gao, F. Xiao, C.B. Ching, H. Duan, ACS Appl. Mater. Interfaces 4 (2012) 2801–2810.
[28] L.F. Chen, Z.H. Huang, H.W. Liang, Q.F. Guan, S.H. Yu, Adv. Mater. 25 (2013) 4746–4752.
[29] X. Lu, M. Yu, G. Wang, T. Zhai, S. Xie, Y. Ling, Y. Tong, Y. Li, Adv. Mater. 25 (2013) 267–272.
[30] T. Brousse, M. Toupin, R. Dugas, L. Athouël, O. Crosnier, D. Belanger, J. Electrochem. Soc. 153 (2006) A2171.
[31] S. Devaraj, N. Munichandraiah, J. Phys. Chem. C 112 (2008) 4406–4417.
[32] O. Ghodbane, J.L. Pascal, F. Favier, ACS Appl. Mater. Interfaces 1 (2009) 1130–1139.
[33] C.-L. Xu, S.-J. Bao, L.-B. Kong, H. Li, H.-L. Li, J. Solid State Chem. 179 (2006) 1351–1355.
[34] J. Li, I. Zhitomirsky, Mater. Chem. Phys. 112 (2008) 525–530.
[35] M. Wu, L. Zhang, J. Gao, C. Xiao, D. Wang, A. Chen, S. Zhang, J. Electroanal. Chem. 613 (2008) 125–130.
[36] W. Xiao, H. Xia, J.-Y.-H. Fuh, L. Lu, J. Electrochem. Soc. 156 (2009) A627.
[37] H. Xia, J. Feng, H. Wang, M.O. Lai, L. Lu, J. Power Sources 195 (2010) 4410–4413.
[38] X. Lu, D. Zheng, T. Zhai, Z. Liu, Y. Huang, S. Xie, Y. Tong, Energy Environ. Sci. 4 (2011) 2915.
[39] Y. Zhao, P. Jiang, S.-S. Xie, J. Power Sources 239 (2013) 393–398.
[40] C.D. Lokhande, D.P. Dubal, O.-S. Joo, Curr. Appl. Phys. 11 (2011) 255–270.
[41] J. Jiang, Y. Li, J. Liu, X. Huang, C. Yuan, X.W. Lou, Adv. Mater. 24 (2012) 5166–5180.
[42] J.A. Yan, E. Khoo, A. Sumboja, P.S. Lee, ACS Nano 4 (2010) 4247–4255.
[43] L. Bao, J. Zang, X. Li, Nano Lett. 11 (2011) 1215–1220.
[44] A.E. Fischer, K.A. Pettigrew, D.R. Rolison, R.M. Stroud, J.W. Long, Nano Lett. 7 (2007) 281–286.
[45] H. Zhang, G.P. Cao, Z.Y. Wang, Y.S. Yang, Z.J. Shi, Z.N. Gu, Nano Lett. 8 (2008) 2664–2668.
[46] J.C. Lytle, J.M. Wallace, M.B. Sassin, A.J. Barrow, J.W. Long, J.L. Dysart, C.H. Renninger, M.P. Saunders, N.L. Brandell, D.R. Rolison, Energy Environ. Sci. 4 (2011) 1913.
[47] L. Xingyou, A. Hirata, T. Fujita, C. Mingwei, Nat. Nanotechnol. 6 (2011) 232–236.
[48] L. Hu, M. Pasta, F.L. Mantia, L. Cui, S. Jeong, H.D. Deshazer, J.W. Choi, S.M. Han, Y. Cui, Nano Lett. 10 (2010) 708–714.
[49] X. Xiao, T.Q. Li, P.H. Yang, Y. Gao, H.Y. Jin, W.J. Ni, W.H. Zhan, X.H. Zhang, Y.Z. Cao, J.W. Zhong, L. Gong, W.C. Yen, W.J. Mai, J. Chen, K.F. Huo, Y.L. Chueh, Z.L. Wang, J. Zhou, ACS Nano 6 (2012) 9200–9206.
[50] Z. Gui, H.L. Zhu, E. Gillette, X.G. Han, G.W. Rubloff, L.B. Hu, S.B. Lee, ACS Nano 7 (2013) 6037–6046.
[51] Y. He, W. Chen, C. Gao, J. Zhou, X. Li, E. Xie, Nanoscale 5 (2013) 8799–8820.
[52] X. Cai, M. Peng, X. Yu, Y. Fu, D. Zou, J. Mater. Chem. C 2 (2014) 1184.
[53] P.-C. Chen, G. Shen, S. Sukcharoenchoke, C. Zhou, Appl. Phys. Lett. 94 (2009) 043113.
[54] A. Yu, I. Roes, A. Davies, Z. Chen, Appl. Phys. Lett. 96 (2010) 253105.
[55] H.Y. Jung, M.B. Karimi, M.G. Hahm, P.M. Ajayan, Y.J. Jung, Sci. Rep. 2 (2012) 773.
[56] T. Chen, H. Peng, M. Durstock, L. Dai, Sci. Rep. 4 (2014) 3612.
[57] J. Bae, M.K. Song, Y.J. Park, J.M. Kim, M. Liu, Z.L. Wang, Angew. Chem. Int. Ed. 50 (2011) 1683–1687.
[58] X. Lu, M. Yu, G. Wang, Y. Tong, Y. Li, Energy Environ. Sci. 7 (2014) 2160.
[59] Q. Li, Z.L. Wang, G.R. Li, R. Guo, L.X. Ding, Y.X. Tong, Nano Lett. 12 (2012) 3803–3807.
[60] Z. Sun, S. Firdoz, E.Y. Yap, L. Li, X. Lu, Nanoscale 5 (2013) 4379–4387.
[61] S. Dong, X. Chen, L. Gu, X. Zhou, L. Li, Z. Liu, P. Han, H. Xu, J. Yao, H. Wang, X. Zhang, C. Shang, G. Cui, L. Chen, Energy Environ. Sci. 4 (2011) 3502.
[62] Y.-B. He, G.-R. Li, Z.-L. Wang, C.-Y. Su, Y.-X. Tong, Energy Environ. Sci. 4 (2011) 1288.
[63] J. Liu, J. Jiang, C. Cheng, H. Li, J. Zhang, H. Gong, H.J. Fan, Adv. Mater. 23 (2011) 2076–2081.
[64] X. Lu, G. Wang, T. Zhai, M. Yu, J. Gan, Y. Tong, Y. Li, Nano Lett. 12 (2012) 1690–1696.
[65] J.-G. Wang, Y. Yang, Z.-H. Huang, F. Kang, Electrochim. Acta 56 (2011) 9240–9247.
[66] Y.M. He, W.J. Chen, X.D. Li, Z.X. Zhang, J.C. Fu, C.H. Zhao, E.Q. Xie, ACS Nano 7 (2013) 174–182.
[67] R. Liu, S.B. Lee, J. Am. Chem. Soc. 130 (2008) 2942–2943.
[68] R. Liu, J. Duay, S.B. Lee, ACS Nano 4 (2010) 4299–4307.
[69] R. Liu, J. Duay, S.B. Lee, ACS Nano 5 (2011) 5608–5619.
[70] Y. Gogotsi, P. Simon, Science 334 (2011) 917–918.
[71] M.D. Stoller, R.S. Ruoff, Energy Environ. Sci. 3 (2010) 1294.
[72] X. Zhao, B.M. Sanchez, P.J. Dobson, P.S. Grant, Nanoscale 3 (2011) 839–855.
[73] W. Chen, R.B. Rakhi, L. Hu, X. Xie, Y. Cui, H.N. Alshareef, Nano Lett. 11 (2011) 5165–5172.
[74] L.B. Hu, W. Chen, X. Xie, N.A. Liu, Y. Yang, H. Wu, Y. Yao, M. Pasta, H.N. Alshareef, Y. Cui, ACS Nano 5 (2011) 8904–8913.
[75] P. Lv, P. Zhang, Y. Feng, Y. Li, W. Feng, Electrochim. Acta 78 (2012) 515–523.
[76] J. Yan, Z. Fan, T. Wei, W. Qian, M. Zhang, F. Wei, Carbon 48 (2010) 3825–3833.
[77] A. Burke, Electrochim. Acta 53 (2007) 1083–1091.
[78] J.-G. Wang, Y. Yang, Z.-H. Huang, F. Kang, J. Mater. Chem. 22 (2012) 16943.
[79] J. Tao, N. Liu, L. Li, J. Su, Y. Gao, Nanoscale 6 (2014) 2922–2928.
[80] P. Li, C. Kong, Y. Shang, E. Shi, Y. Yu, W. Qian, F. Wei, J. Wei, K. Wang, H. Zhu, A. Cao, D. Wu, Nanoscale 5 (2013) 8472–8479.
[81] H. Sun, Z. Xu, C. Gao, Adv. Mater. 25 (2013) 2554–2560.
[82] P. Li, Y. Yang, E. Shi, Q. Shen, Y. Shang, S. Wu, J. Wei, K. Wang, H. Zhu, Q. Yuan, A. Cao, D. Wu, ACS Appl. Mater. Interfaces 6 (2014) 5228–5234.
[83] Maxwell, http://www.maxwell.com/products/ultracapacitors/products/hc-series (accessed 30.03. 15.).
[84] L.Y. Yuan, X.H. Lu, X. Xiao, T. Zhai, J.J. Dai, F.C. Zhang, B. Hu, X. Wang, L. Gong, J. Chen, C.G. Hu, Y.X. Tong, J. Zhou, Z.L. Wang, ACS Nano 6 (2012) 656–661.
[85] M.-J. Deng, P.-J. Ho, C.-Z. Song, S.-A. Chen, J.-F. Lee, J.-M. Chen, K.-T. Lu, Energy Environ. Sci. 6 (2013) 2178.
[86] S. He, W. Chen, J. Power Sources 262 (2014) 391–400.
[87] J. Shen, A. Liu, Y. Tu, H. Wang, R. Jiang, J. Ouyang, Y. Chen, Electrochim. Acta 78 (2012) 122–132.
[88] X. Zhang, D. Zhao, Y. Zhao, P. Tang, Y. Shen, C. Xu, H. Li, Y. Xiao, J. Mater. Chem. A 1 (2013) 3706.
[89] Y. Cheng, S. Lu, H. Zhang, C.V. Varanasi, J. Liu, Nano Lett. 12 (2012) 4206–4211.
[90] J.-K. Chang, S.-H. Hsu, W.-T. Tsai, I.W. Sun, J. Power Sources 177 (2008) 676–680.
[91] D. Liu, Q. Wang, L. Qiao, F. Li, D. Wang, Z. Yang, D. He, J. Mater. Chem. 22 (2012) 483.
[92] J. Xiao, S. Yang, L. Wan, F. Xiao, S. Wang, J. Power Sources 245 (2014) 1027–1034.
[93] Y. Lei, B. Daffos, P.L. Taberna, P. Simon, F. Favier, Electrochim. Acta 55 (2010) 7454–7459.
[94] H.J. Qiu, J.L. Kang, P. Liu, A. Hirata, T. Fujita, M.W. Chen, J. Power Sources 247 (2014) 896–905.
[95] C.-L. Ho, M.-S. Wu, J. Phys. Chem. C 115 (2011) 22068–22074.
[96] X.Y. Lang, H.T. Yuan, Y. Iwasa, M.W. Chen, Scr. Mater. 64 (2011) 923–926.

[97] L.Y. Chen, J.L. Kang, Y. Hou, P. Liu, T. Fujita, A. Hirata, M.W. Chen, J. Mater. Chem. A 1 (2013) 9202.
[98] J. Kang, A. Hirata, L. Kang, X. Zhang, Y. Hou, L. Chen, C. Li, T. Fujita, K. Akagi, M. Chen, Angew. Chem. Int. Ed. 52 (2013) 1664–1667.
[99] Y.-L. Chen, P.-C. Chen, T.-L. Chen, C.-Y. Lee, H.-T. Chiu, J. Mater. Chem. A 1 (2013) 13301.
[100] W.B. Yan, T. Ayvazian, J. Kim, Y. Liu, K.C. Donavan, W.D. Xing, Y.G. Yang, J.C. Hemminger, R.M. Penner, ACS Nano 5 (2011) 8275–8287.
[101] W. Yan, J.Y. Kim, W. Xing, K.C. Donavan, T. Ayvazian, R.M. Penner, Chem. Mater. 24 (2012) 2382–2390.
[102] Z. Yu, B. Duong, D. Abbitt, J. Thomas, Adv. Mater. 25 (2013) 3302–3306.
[103] Y. Qiu, Y. Zhao, X. Yang, W. Li, Z. Wei, J. Xiao, S.F. Leung, Q. Lin, H. Wu, Y. Zhang, Z. Fan, S. Yang, Nanoscale 6 (2014) 3626–3631.
[104] D. Zhu, Y. Wang, G. Yuan, H. Xia, Chem. Commun. 50 (2014) 2876–2878.
[105] U. Özgür, Y.I. Alivov, C. Liu, A. Teke, M.A. Reshchikov, S. Dogan, V. Avrutin, S.J. Cho, H. Morkoc, J. Appl. Phys. 98 (2005) 041301.
[106] X. Sun, Q. Li, Y. Lu, Y. Mao, Chem. Commun. 49 (2013) 4456–4458.
[107] P.H. Yang, X. Xiao, Y.Z. Li, Y. Ding, P.F. Qiang, X.H. Tan, W.J. Mai, Z.Y. Lin, W.Z. Wu, T.Q. Li, H.Y. Jin, P.Y. Liu, J. Zhou, C.P. Wong, Z.L. Wang, ACS Nano 7 (2013) 2617–2626.
[108] N. Li, J.-Y. Wang, Z.-Q. Liu, Y.-P. Guo, D.-Y. Wang, Y.-Z. Su, S. Chen, RSC Adv. 4 (2014) 17274.
[109] S. Li, J. Wen, X. Mo, H. Long, H. Wang, J. Wang, G. Fang, J. Power Sources 256 (2014) 206–211.
[110] J. Rodriguez-Moreno, E. Navarrete-Astorga, E.A. Dalchiele, R. Schrebler, J.R. Ramos-Barrado, F. Martin, Chem. Commun. 50 (2014) 5652–5655.
[111] Y. Zhao, P. Jiang, Coll. Surf. A 444 (2014) 232–239.
[112] W. Zilong, Z. Zhu, J. Qiu, S. Yang, J. Mater. Chem. C 2 (2014) 1331.
[113] X. Lu, G. Wang, S. Xie, J. Shi, W. Li, Y. Tong, Y. Li, Chem. Commun. 48 (2012) 7717–7719.
[114] S. Murugesan, P. Kuppusami, N. Parvathavarthini, E. Mohandas, Surf. Coat. Technol. 201 (2007) 7713–7719.
[115] M. Salari, S.H. Aboutalebi, K. Konstantinov, H.K. Liu, Phys. Chem. Chem. Phys. 13 (2011) 5038–5041.
[116] M. Salari, K. Konstantinov, H.K. Liu, J. Mater. Chem. 21 (2011) 5128.
[117] Y. Luo, D. Kong, J. Luo, S. Chen, D. Zhang, K. Qiu, X. Qi, H. Zhang, C.M. Li, T. Yu, RSC Adv. 3 (2013) 14413.
[118] D. Choi, P.N. Kumta, J. Electrochem. Soc. 153 (2006) A2298.
[119] Y. Xie, Y. Wang, H. Du, Mater. Sci. Eng. B 178 (2013) 1443–1451.
[120] S. Dong, X. Chen, L. Gu, X. Zhou, H. Xu, H. Wang, Z. Liu, P. Han, J. Yao, L. Wang, G. Cui, L. Chen, ACS Appl. Mater. Interfaces 3 (2011) 93–98.
[121] Z. Wang, Z. Li, J. Feng, S. Yan, W. Luo, J. Liu, T. Yu, Z. Zou, Phys. Chem. Chem. Phys. 16 (2014) 8521–8528.
[122] Y. Xie, X. Fang, Electrochim. Acta 120 (2014) 273–283.
[123] S.A. Sherrill, J. Duay, Z. Gui, P. Banerjee, G.W. Rubloff, S.B. Lee, Phys. Chem. Chem. Phys. 13 (2011) 15221–15226.
[124] G.D. Moon, J.B. Joo, M. Dahl, H. Jung, Y. Yin, Adv. Funct. Mater. 24 (2014) 848–856.
[125] M. Hamdani, R.N. Singh, P. Chartier, Int. J. Electrochem. Sci. 5 (2010) 556–577.
[126] Y. Gao, S. Chen, D. Cao, G. Wang, J. Yin, J. Power Sources 195 (2010) 1757–1760.
[127] L. Han, P. Tang, L. Zhang, Nano Energy 7 (2014) 42–51.
[128] M. Huang, Y. Zhang, F. Li, L. Zhang, Z. Wen, Q. Liu, J. Power Sources 252 (2014) 98–106.
[129] W. Li, G. Li, J. Sun, R. Zou, K. Xu, Y. Sun, Z. Chen, J. Yang, J. Hu, Nanoscale 5 (2013) 2901–2908.
[130] L. Yu, G. Zhang, C. Yuan, X.W. Lou, Chem. Commun. 49 (2013) 137–139.
[131] K. Xu, W. Li, Q. Liu, B. Li, X. Liu, L. An, Z. Chen, R. Zou, J. Hu, J. Mater. Chem. A 2 (2014) 4795.
[132] F. Grote, L. Wen, Y. Lei, J. Power Sources 256 (2014) 37–42.
[133] D.T. Dam, J.-M. Lee, Nano Energy 2 (2013) 933–942.
[134] J.S. Kim, S.S. Shin, H.S. Han, L.S. Oh, D.H. Kim, J.H. Kim, K.S. Hong, J.Y. Kim, ACS Appl. Mater. Interfaces 6 (2014) 268–274.
[135] X. Lu, T. Zhai, X. Zhang, Y. Shen, L. Yuan, B. Hu, L. Gong, J. Chen, Y. Gao, J. Zhou, Y. Tong, Z.L. Wang, Adv. Mater. 24 (2012) 938–944.
[136] S. Talapatra, S. Kar, S.K. Pal, R. Vajtai, L. Ci, P. Victor, M.M. Shaijumon, S. Kaur, O. Nalamasu, P.M. Ajayan, Nat. Nanotechnol. 1 (2006) 112–116.
[137] Z. Fan, J. Chen, B. Zhang, B. Liu, X. Zhong, Y. Kuang, Diam. Relat. Mater. 17 (2008) 1943–1948.
[138] R. Amade, E. Jover, B. Caglar, T. Mutlu, E. Bertran, J. Power Sources 196 (2011) 5779–5783.
[139] P. Lv, Y.Y. Feng, Y. Li, W. Feng, J. Power Sources 220 (2012) 160–168.
[140] A.L.M. Reddy, M.M. Shaijumon, S.R. Gowda, P.M. Ajayan, J. Phys. Chem. C 114 (2010) 658–663.
[141] Q. Li, X.F. Lu, H. Xu, Y.X. Tong, G.R. Li, ACS Appl. Mater. Interfaces 6 (2014) 2726–2733.
[142] Y. Wang, H. Liu, X. Sun, I. Zhitomirsky, Scr. Mater. 61 (2009) 1079–1082.
[143] G. Mo, Y. Zhang, W. Zhang, J. Ye, Electrochim. Acta 113 (2013) 373–381.
[144] T. Bordjiba, D. Bélanger, Electrochim. Acta 55 (2010) 3428–3433.
[145] S.W. Lee, J. Kim, S. Chen, P.T. Hammond, Y. Shao-Horn, ACS Nano 4 (2010) 3889–3896.
[146] K.-W. Nam, C.-W. Lee, X.-Q. Yang, B.W. Cho, W.-S. Yoon, K.-B. Kim, J. Power Sources 188 (2009) 323–331.
[147] S.-L. Chou, J.-Z. Wang, S.-Y. Chew, H.-K. Liu, S.-X. Dou, Electrochem. Commun. 10 (2008) 1724–1727.
[148] Y. Jin, H. Chen, M. Chen, N. Liu, Q. Li, ACS Appl. Mater. Interfaces 5 (2013) 3408–3416.
[149] K.S. Novoselov, A.K. Geim, S.V. Morozov, D. Jiang, Y. Zhang, S.V. Dubonos, I.V. Grigorieva, A.A. Firsov, Science 306 (2004) 666–669.
[150] Z.-S. Wu, G. Zhou, L.-C. Yin, W. Ren, F. Li, H.-M. Cheng, Nano Energy 1 (2012) 107–131.
[151] L. Jiang, Z. Fan, Nanoscale 6 (2014) 1922–1945.
[152] D. Chen, L. Tang, J. Li, Chem. Soc. Rev. 39 (2010) 3157–3180.
[153] Y. Xu, G. Shi, J. Mater. Chem. 21 (2011) 3311.
[154] Z. Dong, C. Jiang, H. Cheng, Y. Zhao, G. Shi, L. Jiang, L. Qu, Adv. Mater. 24 (2012) 1856–1861.
[155] Z. Xu, H. Sun, X. Zhao, C. Gao, Adv. Mater. 25 (2013) 188–193.
[156] Q. Chen, Y. Meng, C. Hu, Y. Zhao, H. Shao, N. Chen, L. Qu, J. Power Sources 247 (2014) 32–39.
[157] B. Zheng, T. Huang, L. Kou, X. Zhao, K. Gopalsamy, C. Gao, J. Mater. Chem. A (2014). Q5
[158] Q. Cheng, J. Tang, J. Ma, H. Zhang, N. Shinya, L.-C. Qin, Carbon 49 (2011) 2917–2925.
[159] B.G. Choi, Y.S. Huh, W.H. Hong, H.J. Kim, H.S. Park, Nanoscale 4 (2012) 5394–5400.
[160] X. Yang, C. Cheng, Y. Wang, L. Qiu, D. Li, Science 341 (2013) 534–537.
[161] Z. Li, Y. Mi, X. Liu, S. Liu, S. Yang, J. Wang, J. Mater. Chem. 21 (2011) 14706.
[162] S. Wu, W. Chen, L. Yan, J. Mater. Chem. A 2 (2014) 2765.
[163] T. Zhai, F. Wang, M. Yu, S. Xie, C. Liang, C. Li, F. Xiao, R. Tang, Q. Wu, X. Lu, Y. Tong, Nanoscale 5 (2013) 6790–6796.
[164] Z.P. Chen, W.C. Ren, L.B. Gao, B.L. Liu, S.F. Pei, H.M. Cheng, Nat. Mater. 10 (2011) 424–428.
[165] X. Dong, X. Wang, J. Wang, H. Song, X. Li, L. Wang, M.B. Chan-Park, C.M. Li, P. Chen, Carbon 50 (2012) 4865–4870.
[166] U.M. Patil, J.S. Sohn, S.B. Kulkarni, H.G. Park, Y. Jung, K.V. Gurav, J.H. Kim, S.C. Jun, Mater. Lett. 119 (2014) 135–139.
[167] D. Li, Y.N. Xia, Adv. Mater. 16 (2004) 1151–1170.
[168] Y.-C. Chen, Y.-K. Hsu, Y.-G. Lin, Y.-K. Lin, Y.-Y. Horng, L.-C. Chen, K.-H. Chen, Electrochim. Acta 56 (2011) 7124–7130.
[169] J. Tao, N. Liu, W. Ma, L. Ding, L. Li, J. Su, Y. Gao, Sci. Rep. 3 (2013) 2286.
[170] M. Yu, T. Zhai, X. Lu, X. Chen, S. Xie, W. Li, C. Liang, W. Zhao, L. Zhang, Y. Tong, J. Power Sources 239 (2013) 64–71.
[171] P. Yang, Y. Li, Z. Lin, Y. Ding, S. Yue, C.P. Wong, X. Cai, S. Tan, W. Mai, J. Mater. Chem. A 2 (2014) 595.
[172] D. Guo, X. Yu, W. Shi, Y. Luo, Q. Li, T. Wang, J. Mater. Chem. A 2 (2014) 8833.
[173] Y. Luo, J. Jiang, W. Zhou, H. Yang, J. Luo, X. Qi, H. Zhang, D.Y.W. Yu, C.M. Li, T. Yu, J. Mater. Chem. 22 (2012) 8634.
[174] J.-G. Wang, Y. Yang, Z.-H. Huang, F. Kang, Electrochim. Acta 75 (2012) 213–219.
[175] M. Zhi, A. Manivannan, F. Meng, N. Wu, J. Power Sources 208 (2012) 345–353.
[176] J. Liu, J. Essner, J. Li, Chem. Mater. 22 (2010) 5022–5030.
[177] G. Xiong, K.P.S.S. Hembram, R.G. Reifenberger, T.S. Fisher, J. Power Sources 227 (2013) 254–259.
[178] S. Hassan, M. Suzuki, S. Mori, A.A. El-Moneim, J. Power Sources 249 (2014) 21–27.
[179] S. Hassan, M. Suzuki, S. Mori, A.A. El-Moneim, RSC Adv. 4 (2014) 20479.
[180] M.B. Sassin, C.P. Hoag, B.T. Willis, N.W. Kucko, D.R. Rolison, J.W. Long, Nanoscale 5 (2013) 1649–1657.
[181] T. Bordjiba, D. Belanger, J. Electrochem. Soc. 156 (2009) A378.
[182] W. Chen, Y. He, X. Li, J. Zhou, Z. Zhang, C. Zhao, C. Gong, S. Li, X. Pan, E. Xie, Nanoscale 5 (2013) 11733–11741.
[183] Y. He, W. Chen, J. Zhou, X. Li, P. Tang, Z. Zhang, J. Fu, E. Xie, ACS Appl. Mater. Interfaces 6 (2014) 210–218.
[184] G. Zhu, Z. He, J. Chen, J. Zhao, X. Feng, Y. Ma, Q. Fan, L. Wang, W. Huang, Nanoscale 6 (2014) 1079–1085.
[185] Y. Gao, Y.S. Zhou, M. Qian, H.M. Li, J. Redepenning, L.S. Fan, X.N. He, W. Xiong, X. Huang, M. Majhouri-Samani, L. Jiang, Y.F. Lu, RSC Adv. 3 (2013) 20613.
[186] S.-M. Li, Y.-S. Wang, S.-Y. Yang, C.-H. Liu, K.-H. Chang, H.-W. Tien, N.-T. Wen, C.-C.M. Ma, C.-C. Hu, J. Power Sources 225 (2013) 347–355.
[187] Y. Wang, J. Chen, J. Cao, Y. Liu, Y. Zhou, J.-H. Ouyang, D. Jia, J. Power Sources 271 (2014) 269–277.
[188] G. Yu, L. Hu, N. Liu, H. Wang, M. Vosgueritchian, Y. Yang, Y. Cui, Z. Bao, Nano Lett. 11 (2011) 4438–4442.
[189] Z.L. Wang, R. Guo, L.X. Ding, Y.X. Tong, G.R. Li, Sci. Rep. 3 (2013) 1204.
[190] Z. Yu, C. Li, D. Abbitt, J. Thomas, J. Mater. Chem. A (2014).
[191] J. Duay, E. Gillette, R. Liu, S.B. Lee, Phys. Chem. Chem. Phys. 14 (2012) 3329–3337.
[192] G. Yu, L. Hu, M. Vosgueritchian, H. Wang, X. Xie, J.R. McDonough, X. Cui, Y. Cui, Z. Bao, Nano Lett. 11 (2011) 2905–2911.
[193] W. Chen, R.B. Rakhi, H.N. Alshareef, J. Mater. Chem. 22 (2012) 14394.
[194] J. Ge, H.-B. Yao, W. Hu, X.-F. Yu, Y.-X. Yan, L.-B. Mao, H.-H. Li, S.-S. Li, S.-H. Yu, Nano Energy 2 (2013) 505–513.
[195] W. Jiang, K. Zhang, L. Wei, D. Yu, J. Wei, Y. Chen, Nanoscale 5 (2013) 11108–11117.
[196] J. Xu, H. Wu, C. Xu, H. Huang, L. Lu, G. Ding, H. Wang, D. Liu, G. Shen, D. Li, X. Chen, Chem. Eur. J. 19 (2013) 6451–6458.
[197] J.-X. Feng, Q. Li, X.-F. Lu, Y.-X. Tong, G.-R. Li, J. Mater. Chem. A 2 (2014) 2985.
[198] T. Ohzuku, M. Kitagawa, T. Hirai, J. Electrochem. Soc. 136 (1989) 3169–3174.

[199] J.P. Rethinaraj, S. Visvanathan, J. Power Sources 42 (1993) 335–343.
[200] S.C. Pang, M.A. Anderson, J. Mater. Res. 15 (2000) 2096–2106.
[201] C.C. Hu, T.W. Tsou, Electrochem. Commun. 4 (2002) 105–109.
[202] C.C. Hu, T.W. Tsou, Electrochim. Acta 47 (2002) 3523–3532.
[203] J.-K. Chang, W.-T. Tsai, J. Electrochem. Soc. 150 (2003) A1333.
[204] C.-C. Hu, T.-W. Tsou, J. Power Sources 115 (2003) 179–186.
[205] C.-C. Hu, C.-C. Wang, J. Electrochem. Soc. 150 (2003) A1079.
[206] J.-K. Chang, Y.-L. Chen, W.-T. Tsai, J. Power Sources 135 (2004) 344–353.
[207] J.-K. Chang, C.-T. Lin, W.-T. Tsai, Electrochem. Commun. 6 (2004) 666–671.
[208] Y.-S. Chen, C.-C. Hu, Y.-T. Wu, J. Solid State Electrochem. 8 (2004) 467–473.
[209] J.-K. Chang, W.-T. Tsai, J. Electrochem. Soc. 152 (2005) A2063.
[210] T. Shinomiya, V. Gupta, N. Miura, Electrochim. Acta 51 (2006) 4412–4419.
[211] J.K. Chang, W.T. Tsai, J. Appl. Electrochem. 34 (2004) 953–961.
[212] C.-C. Hu, K.-H. Chang, Y.-T. Wu, C.-Y. Hung, C.-C. Lin, Y.-T. Tsai, Electrochem. Commun. 10 (2008) 1792–1796.
[213] C.-C. Hu, C.-Y. Hung, K.-H. Chang, Y.-L. Yang, J. Power Sources 196 (2011) 847–850.
[214] H. Liu, B. Lu, S. Wei, M. Bao, Y. Wen, F. Wang, Solid State Sci. 14 (2012) 789–793.
[215] J. Duay, S.A. Sherrill, Z. Gui, E. Gillette, S.B. Lee, ACS Nano 7 (2013) 1200–1214.
[216] W. Wei, X. Cui, X. Mao, W. Chen, D.G. Ivey, Electrochim. Acta 56 (2011) 1619–1628.
[217] P.Y. Tang, Y.Q. Zhao, Y.M. Wang, C.L. Xu, Nanoscale 5 (2013) 8156–8163.
[218] M. Nakayama, T. Kanaya, R. Inoue, Electrochem. Commun. 9 (2007) 1154–1158.
[219] T.M. Benedetti, V.R. Gonçales, S.I. Córdoba de Torresi, R.M. Torresi, J. Power Sources 239 (2013) 1–8.
[220] K. SainanYang, J. Cheng, K. Huang, Y. Ye, D. Xu, X.Z.G. Cao, Wang, Electrochim. Acta 120 (2014) 416–422.
[221] C.J. Clarke, G.J. Browning, S.W. Donne, Electrochim. Acta 51 (2006) 5773–5784.
[222] A.D. Cross, I. Olcomendy, M. Drozd, A.F. Hollenkamp, S.W. Donne, J. Electrochem. Soc. 160 (2012) A368–A375.
[223] M.F. Dupont, S.W. Donne, Electrochim. Acta 120 (2014) 219–225.
[224] M. Shamoto, K. Mori, K. Tomono, M. Nakayama, J. Electrochem. Soc. 160 (2013) D132–D136.
[225] J.N. Broughton, M.J. Brett, Electrochim. Acta 50 (2005) 4814–4819.
[226] Y.-L. Wang, Y.-Q. Zhao, C.-L. Xu, J. Solid State Electrochem. 16 (2011) 829–834.
[227] L.-B. Kong, R.-J. Bai, J.-W. Lang, Y.-C. Luo, L. Kang, Russ. J. Electrochem. 49 (2013) 975–982.
[228] G.-Y. Zhao, C.-L. Xu, H.-L. Li, J. Power Sources 163 (2007) 1132–1136.
[229] G.M. Jacob, I. Zhitomirsky, Appl. Surf. Sci. 254 (2008) 6671–6676.
[230] M. Nakayama, M. Nishiyama, M. Shamoto, T. Tanimoto, K. Tomono, R. Inoue, J. Electrochem. Soc. 159 (2012) A1176–A1182.
[231] N. Nagarajan, H. Humadi, I. Zhitomirsky, Electrochim. Acta 51 (2006) 3039–3045.
[232] M. Wu, G.A. Snook, G.Z. Chen, D.J. Fray, Electrochem. Commun. 6 (2004) 499–504.
[233] X. Dong, W. Shen, J. Gu, L. Xiong, Y. Zhu, H. Li, J. Shi, Microporous Mesoporous Mater. 91 (2006) 120–127.
[234] X.P. Dong, W.H. Shen, J.L. Gu, L.M. Xiong, Y.F. Zhu, Z. Li, J.L. Shi, J. Phys. Chem. B 110 (2006) 6015–6019.
[235] S.-B. Ma, Y.-H. Lee, K.-Y. Ahn, C.-M. Kim, K.-H. Oh, K.-B. Kim, J. Electrochem. Soc. 153 (2006) C27.
[236] X. Huang, H. Yue, A. Attia, Y. Yang, J. Electrochem. Soc. 154 (2007) A26.
[237] X. Jin, W. Zhou, S. Zhang, G.Z. Chen, Small 3 (2007) 1513–1517.
[238] S.-B. Ma, K.-Y. Ahn, E.-S. Lee, K.-H. Oh, K.-B. Kim, Carbon 45 (2007) 375–382.
[239] J. Yan, Z. Fan, T. Wei, J. Cheng, B. Shao, K. Wang, L. Song, M. Zhang, J. Power Sources 194 (2009) 1202–1207.
[240] H.-Y. Chu, Q.-Y. Lai, L. Wang, J.-F. Lu, Y. Zhao, Ionics 16 (2010) 233–238.
[241] M.N. Patel, X. Wang, B. Wilson, D.A. Ferrer, S. Dai, K.J. Stevenson, K.P. Johnston, J. Mater. Chem. 20 (2010) 390.
[242] S. Zhang, C. Peng, K.C. Ng, G.Z. Chen, Electrochim. Acta 55 (2010) 7447–7453.
[243] Y. Peng, Z. Chen, J. Wen, Q. Xiao, D. Weng, S. He, H. Geng, Y. Lu, Nano Res. 4 (2011) 216–225.
[244] A.E. Fischer, M.P. Saunders, K.A. Pettigrew, D.R. Rolison, J.W. Long, J. Electrochem. Soc. 155 (2008) A246–A252.
[245] B.G. Choi, M. Yang, W.H. Hong, J.W. Choi, Y.S. Huh, ACS Nano 6 (2012) 4020–4028.
[246] H.Z. Chi, S. Tian, X. Hu, H. Qin, J. Xi, J. Alloys Compd. 587 (2014) 354–360.
[247] L. Zhao, J. Yu, W. Li, S. Wang, C. Dai, J. Wu, X. Bai, C. Zhi, Nano Energy 4 (2014) 39–48.
[248] J. Liu, J. Jiang, M. Bosman, H.J. Fan, J. Mater. Chem. 22 (2012) 2419.
[249] R.J. Chen, P. Zavalij, M.S. Whittingham, Chem. Mater. 8 (1996) 1275–1280.
[250] H. Xia, Y. Wang, J. Lin, L. Lu, Nanoscale Res. Lett. 7 (2012) 33.
[251] Y. Chen, Y. Zhang, D. Geng, R. Li, H. Hong, J. Chen, X. Sun, Carbon 49 (2011) 4434–4442.
[252] S.-W. Lee, S.-M. Bak, C.-W. Lee, C. Jaye, D.A. Fischer, B.-K. Kim, X.-Q. Yang, K.-W. Nam, K.-B. Kim, J. Phys. Chem. C 118 (2014) 2834–2843.
[253] X. Li, B. Wei, Nano Energy 1 (2012) 479–487.
[254] Y. Hu, J. Wang, X. Jiang, Y. Zheng, Z. Chen, Appl. Surf. Sci. 271 (2013) 193–201.
[255] X. Wang, H. Liu, X. Chen, D.G. Evans, W. Yang, Electrochim. Acta 78 (2012) 115–121.
[256] R. Huang, J. Zhu, R. Yu, Chin. Phys. B 18 (2009) 3024–3030.
[257] J.H. Noh, H.S. Han, S. Lee, J.Y. Kim, K.S. Hong, G.S. Han, H. Shin, H.S. Jung, Adv. Energy Mater. 1 (2011) 829–835.
[258] A. Adeyemo, G. Hunter, P.K. Dutta, Sens. Actuator B Chem. 152 (2011) 307–315.
[259] D. Choi, G.E. Blomgren, P.N. Kumta, Adv. Mater. 18 (2006) 1178–1182.

Please cite this article in press as: J. Cao, et al., Journal of Power Sources (2015), http://dx.doi.org/10.1016/j.jpowsour.2015.05.115